Calhoun: The NPS Institutional Archive

DSpace Repository

Theses and Dissertations | 1. Thesis and Dissertation Collection, all items

2017-12

Actinide isotope ratios measured by Resonance Ionization Mass Spectrometry: optimization of ionization schemes and demonstration using nuclear fallout

Brewster, Drake E.

Monterey, California: Naval Postgraduate School

https://hdl.handle.net/10945/56870

This publication is a work of the U.S. Government as defined in Title 17, United States Code, Section 101. Copyright protection is not available for this work in the United States.

Downloaded from NPS Archive: Calhoun

http://www.nps.edu/library

Calhoun is the Naval Postgraduate School's public access digital repository for research materials and institutional publications created by the NPS community. Calhoun is named for Professor of Mathematics Guy K. Calhoun, NPS's first appointed -- and published -- scholarly author.

Dudley Knox Library / Naval Postgraduate School
411 Dyer Road / 1 University Circle
Monterey, California USA 93943

NAVAL POSTGRADUATE SCHOOL

MONTEREY, CALIFORNIA

THESIS

ACTINIDE ISOTOPE RATIOS MEASURED BY RESONANCE IONIZATION MASS SPECTROMETRY: OPTIMIZATION OF IONIZATION SCHEMES AND DEMONSTRATION USING NUCLEAR FALLOUT

by

Drake E. Brewster

December 2017

Thesis Advisor: Craig F. Smith
Second Reader: Brett H. Isselhardt

Approved for public release. Distribution is unlimited.

THIS PAGE INTENTIONALLY LEFT BLANK

REPORT DOCUMENTATION PAGE			*Form Approved OMB No. 0704–0188*

Public reporting burden for this collection of information is estimated to average 1 hour per response, including the time for reviewing instruction, searching existing data sources, gathering and maintaining the data needed, and completing and reviewing the collection of information. Send comments regarding this burden estimate or any other aspect of this collection of information, including suggestions for reducing this burden, to Washington headquarters Services, Directorate for Information Operations and Reports, 1215 Jefferson Davis Highway, Suite 1204, Arlington, VA 22202-4302, and to the Office of Management and Budget, Paperwork Reduction Project (0704-0188) Washington, DC 20503.

1. AGENCY USE ONLY *(Leave blank)*	**2. REPORT DATE** December 2017	**3. REPORT TYPE AND DATES COVERED** Master's Thesis

4. TITLE AND SUBTITLE ACTINIDE ISOTOPE RATIOS MEASURED BY RESONANCE IONIZATION MASS SPECTROMETRY: OPTIMIZATION OF IONIZATION SCHEMES AND DEMONSTRATION USING NUCLEAR FALLOUT	**5. FUNDING NUMBERS**
6. AUTHOR(S) Drake E. Brewster	
7. PERFORMING ORGANIZATION NAME(S) AND ADDRESS(ES) Naval Postgraduate School Monterey, CA 93943-5000	**8. PERFORMING ORGANIZATION REPORT NUMBER**
9. SPONSORING /MONITORING AGENCY NAME(S) AND ADDRESS(ES) N/A	**10. SPONSORING / MONITORING AGENCY REPORT NUMBER**

11. SUPPLEMENTARY NOTES The views expressed in this thesis are those of the author and do not reflect the official policy or position of the Department of Defense or the U.S. Government. IRB number ____N/A____.

12a. DISTRIBUTION / AVAILABILITY STATEMENT Approved for public release. Distribution is unlimited.	**12b. DISTRIBUTION CODE**

13. ABSTRACT (maximum 200 words)

Resonance Ionization Mass Spectrometry is a technology for analysis of isotopic composition of samples that was developed as early as the 1980s. Since its development, technological advancements have enabled instruments such as the Laser Ionization of Neutrals instrument at Lawrence Livermore National Laboratory to deliver high yield isotope ratios with an accuracy within 1% at high measurement efficiency while remaining relatively free of isobaric interferences. The instrument has recently been successfully used to quantify uranium isotope ratios in nuclear fallout debris.

The work in this thesis explored three pathways necessary for the development of a field deployable instrument. The first pathway addressed was a feasibility study that showed current continuous wave laser technology incompatible with the ionization approach taken in the current Laser Ionization of Neutrals instrument. Next, new one- and two-color uranium resonance ionization schemes were tested that showed an increase in uranium signal by 62% by accessing a low-lying excited state. The final experimental investigation studied the effects of carbon coating and implantation on nuclear fallout samples, showing a factor of two increase in the signal-to-noise ratio achieved during measurement of uranium isotope ratios.

14. SUBJECT TERMS Resonance Ionization Mass Spectroscopy, RIMS	**15. NUMBER OF PAGES** 97
	16. PRICE CODE

17. SECURITY CLASSIFICATION OF REPORT	**18. SECURITY CLASSIFICATION OF THIS PAGE**	**19. SECURITY CLASSIFICATION OF ABSTRACT**	**20. LIMITATION OF ABSTRACT**
Unclassified	Unclassified	Unclassified	UU

NSN 7540–01-280-5500 Standard Form 298 (Rev. 2–89) Prescribed by ANSI Std. 239–18

THIS PAGE INTENTIONALLY LEFT BLANK

Approved for public release. Distribution is unlimited.

ACTINIDE ISOTOPE RATIOS MEASURED BY RESONANCE IONIZATION MASS SPECTROMETRY: OPTIMIZATION OF IONIZATION SCHEMES AND DEMONSTRATION USING NUCLEAR FALLOUT

Drake E. Brewster
Captain, United States Army
B.S., Western Illinois University, 2009

Submitted in partial fulfillment of the
requirements for the degree of

MASTER OF SCIENCE IN PHYSICS

from the

NAVAL POSTGRADUATE SCHOOL
December 2017

Approved by: Craig F. Smith
Thesis Advisor

Brett H. Isselhardt
Second Reader, Lawrence Livermore National Laboratory

Kevin B. Smith
Chair, Department of Physics

THIS PAGE INTENTIONALLY LEFT BLANK

ABSTRACT

Resonance Ionization Mass Spectrometry is a technology for analysis of isotopic composition of samples that was developed as early as the 1980s. Since its development, technological advancements have enabled instruments such as the Laser Ionization of Neutrals instrument at Lawrence Livermore National Laboratory to deliver high yield isotope ratios with an accuracy within 1% at high measurement efficiency while remaining relatively free of isobaric interferences. The instrument has recently been successfully used to quantify uranium isotope ratios in nuclear fallout debris.

The work in this thesis explored three pathways necessary for the development of a field deployable instrument. The first pathway addressed was a feasibility study that showed current continuous wave laser technology incompatible with the ionization approach taken in the current Laser Ionization of Neutrals instrument. Next, new one- and two-color uranium resonance ionization schemes were tested that showed an increase in uranium signal by 62% by accessing a low-lying excited state. The final experimental investigation studied the effects of carbon coating and implantation on nuclear fallout samples, showing a factor of two increase in the signal-to-noise ratio achieved during measurement of uranium isotope ratios.

THIS PAGE INTENTIONALLY LEFT BLANK

TABLE OF CONTENTS

I. INTRODUCTION 1
A. SUMMARY OF WORK INCLUDED 1
B. INTRODUCTORY VIGNETTE 2
C. DEFINITION OF NUCLEAR FORENSICS 2
D. EXISTING PROBLEM 2
E. A BRIEF HISTORY OF RIMS 3

II. THEORY 9
A. LASER RESONANCE IONIZATION 9
1. Rate Equations 9
2. The Time-Dependent Schrödinger Equation 12
3. Stimulated Excitation to Bound States 13
4. Ionization Processes 14
B. NUCLEAR FALLOUT DEBRIS FORMATION 17
C. ATOMIZATION OF MATERIAL 21
1. Laser Ablation 21
2. Ion Sputtering 26

III. METHOD 29
A. STEP ONE—ATOMIZATION 29
B. STEP TWO—RESONANCE IONIZATION 33
C. STEP THREE—MASS ANALYSIS AND ION DETECTION 34

IV. EXPERIMENTATION 39
A. CW LASER FEASIBILITY STUDY 39
1. Setup 41
2. Procedure 42
3. Measurement 43
4. Analysis 44
5. Conclusion 47
B. SIMPLIFIED IONIZATION SCHEMES FOR URANIUM 48
1. Setup 49
2. Procedure 50
3. Measurement 51
4. Analysis 54
5. Conclusion 55

C. SURFACE REDUCTION USING CARBON COATING AND IMPLANTATION 56
1. Setup 60
2. Procedure 61
3. Measurement 62
4. Analysis 67
5. Conclusion 68

V. CONCLUSION 69
A. CONTRIBUTIONS OF THIS WORK 69
B. FUTURE RESEARCH OPPORTUNITIES 70
1. Continuous Wave Laser Research 70
2. Two-Color Uranium Resonance Ionization 70
3. Carbon Surface Reduction 71

LIST OF REFERENCES 73

INITIAL DISTRIBUTION LIST 77

LIST OF FIGURES

Figure 1. RIMS measurement of uranium and plutonium isotope ratios simultaneously on the LION Instrument at LLNL. Source: [8].....7

Figure 2. The rate equations illustrated as vectors for a two-state quantum mechanical oscillator located in a radiation field. 11

Figure 3. Two state atomic model with excited state bandwidth of Γ.....13

Figure 4. A depiction of the three ionization processes used in resonance ionization. Source: [7].....15

Figure 5. Spectra of excitation above the ionization potential for ^{238}U from different intermediate states with different angular momentum, $J = 6,7,8$. Source: [11].....15

Figure 6. Fallout formation model. Source: [13].....18

Figure 7. Categorization of fallout samples by size, gamma activity, shape, and color from Operation Plumbbob. Source: [14]. 19

Figure 8. Nuclear fallout debris under scanning electron microscope (SEM). Sample is polished to the mid-plain and embedded in epoxy. Actual sample obtained from Weisz [12]. 21

Figure 9. 2D representation of SiO_2 forming the SiO_4 tetrahedron in its solid-state form. 22

Figure 10. A 2D representation of an a-SiO_2 structure. 23

Figure 11. Plot of valence and conduction bands on energy versus momentum graph. 24

Figure 12. Electron-hole excitation and interaction process depicted on an energy-versus-momentum graph. 25

Figure 13. Plot of the energy of light versus transmission in amorphous-silicon dioxide substrates with thicknesses of 436, 1100, and 5110 angstroms. Original x-axis in eV, author placed second x-axis in nm. Source: [16].....26

Figure 14. Simplified diagram of ion sputtering. Source: [19]. 28

Figure 15. Sample crushed and pressed into iridium on a half-inch target pedestal. 29

Figure 16. Uranium-oxide standard, sample CRM125A, immobilized on carbon double-sided tape on an aluminum pedestal. The sample is shown in the target chamber of LION. 30

Figure 17. LION instrument target chamber during operation. Labeling added. Source: [20]. 31

Figure 18. Uranium 3-color excitation scheme. Source: [22]. 34

Figure 19. Diagram of the TOF-MS depicting target, ion optics, reflectron, and detector. Source: [8]. 34

Figure 20. Illustration of reflectron effect in the TOF-MS. 35

Figure 21. Illustration of the uncertainties incurred by the random velocities and laser ionization beam volume. 37

Figure 22. Mass spectra using the LION instrument with lasers tuned to plutonium (Green), uranium (Red), and off-resonance (Blue). Source: [8]. 38

Figure 23. Picture of the Sacher Lasertechnik COTS CW laser cavity (orange) versus custom built Ti:Saph cavities (yellow). 40

Figure 24. 3-Color Pu resonance ionization scheme showing angular momenta on the left side and the energy in wavenumber on the right side. The second excitation step of this scheme was replaced by a CW laser for this experimental investigation. 41

Figure 25. Plutonium mass spectrum of CRM137 prior to CW versus background experimentation to ensure proper LION instrument operation. 42

Figure 26. CW to background results of six measurements. Table insert shows the total counts summed over the six experiments with the associated standard deviation. 44

Figure 27. Laser saturation curve for plutonium isotopes. Green lines added by author. Green solid line indicates useful power delivered by Sacher Lasertechnik CW laser at 1.16 W. Green dashed line indicates useful power delivered by a Ti:Saph pulsed laser at an average power of 350 mW. Source: [23]. 46

Figure 28. One and two-color uranium laser resonance ionization schemes shown with the utilized excited state and ionization levels with associated energy in wavelength. The 396 nm scheme populates a possible AI state above the IP. The 406 nm scheme populates a

possible Rydberg state below the IP. The Rydberg state is ionized by the shift in the IP caused by the ion extraction field. 50

Figure 29. Saturation curve of one-color uranium scheme. Red Points: Experimental Data. Blue Line: Line Fit. 52

Figure 30. Saturation curve of two-color uranium scheme varying the low-lying state laser (496 nm). A 396 nm laser was held constant at 650 mW. Red Points: Experimental Data. Blue Line: Line Fit. 53

Figure 31. One- and two-color saturation curves for uranium using a known sample; CRM125A. Black: 396 nm alone. Blue: 406 nm varied with 396 nm held constant and normalized to 1 from the 396 nm laser. Red: normalization count line for 406 nm saturation curve. 55

Figure 32. SEM mapping of multiple elements in Sample 1. First Row Si, O, Na, Ca. Second Row K, Ti, Fe, Mg. 57

Figure 33. Mass spectrum of the atomic and molecular uranium region from initial carbon coating test of Sample 1. 58

Figure 34. Mass spectrum of the atomic uranium region from initial carbon coating testing of Sample 1. 58

Figure 35. A graph of $^{234}U/^{235}U$ ratio versus $^{235}U/^{238}U$ ratio. Gold star and arrow added to represent the data collected by LION. The uncertainty is on the order of the symbol size. Source [12]. 58

Figure 36. SEM image of Sample 1 after initial testing. Laser ablation scars appear as dark marks where carbon was removed. 59

Figure 37. SEM image of Sample 2 prior to testing. 60

Figure 38. Mass spectrum of Sample 1 and 2 with carbon coating. Large graph spans 55–270 AMU. Smaller graph shows the uranium region of interest 230–270 AMU. Black: Sample 1 and Red: Sample 2. 63

Figure 39. A SEM image of Sample 1 showing laser ablation scarring caused during laser ablation of a carbon coating. 64

Figure 40. A SEM image of Sample 2 showing laser ablation scarring caused during laser ablation of a carbon coating. 64

Figure 41. SEM image of nuclear fallout Sample 1 after Ar^+ cleaning. Dose of 1.76×10^{16} Ions/cm^2 65

Figure 42. SEM image of Sample 1 after carbon implantation. Total dose of 5.95×10^{16} Ions/cm^2.....66

Figure 43. Mass spectrum of Sample 1 during a carbon implantation experiment with table of ^{235}U counts, ^{238}U counts, noise counts, signal-to-noise ratio included. Black: After Ar^+ sputtering. Blue: 4 minutes methane ion sputtering (Shifted right .5 AMU). Red: 8 minutes total methane ion sputtering (Shifted right 1 AMU). 67

LIST OF TABLES

Table 1. Comparison of the measured average power for a broadband pulsed .298 W laser operating at 1 kHz with a 20 ns pulse versus a 1.16 W narrowband CW laser to the useful energy delivered to the target isotope. 45

Table 2. Laser power versus ion counts for 396 nm one-color two-photon uranium excitation scheme. The final column is normalized to 1 for the highest count achieved. 51

Table 3. Laser power versus ion counts for the low-lying state uranium excitation scheme. The final column is normalized to 1 for the highest count achieved. 53

Table 4. Uranium ion signal from 396 nm, 406 nm, and then both on CRM125A uranium sample. 54

THIS PAGE INTENTIONALLY LEFT BLANK

LIST OF ACRONYMS AND ABBREVIATIONS

AI	Auto-Ionizing
AMU	Atomic Mass Unit
COTS	Commercial Off-the-Shelf
CW	Continuous-Wave
FWHM	Full Width Half Measure
IP	Ionization Potential
LION	Laser Ionization of Neutrals
LLNL	Lawrence Livermore National Laboratory
NPS	Naval Postgraduate School
RIMS	Resonance Ionization Mass Spectrometry
RIS	Resonance Ionization Spectroscopy
SEM	Secondary Electron Microscope
SIMS	Secondary Ion Mass Spectrometry
SNM	Special Nuclear Material
TDC	Time to Digital Converter
Ti:Saph	Titanium Sapphire
TOF-MS	Time-of-Flight Mass Spectrometry

THIS PAGE INTENTIONALLY LEFT BLANK

ACKNOWLEDGMENTS

Thank you to my two advisors for the academic fulfillment and professional development I received. Dr. Craig Smith was an outstanding principal investigator and consistently delivered the guidance necessary for success in this research. Dr. Brett Isselhardt granted unlimited access to his instrument and delivered outstanding mentoring.

Thank you to Dr. Michael Savina and Dr. Reto Trappitsch from the Laser Ionization of Neutrals team. You are true professionals in every aspect of your profession.

The Defense Threat Reduction Agency is gratefully acknowledged for its funding and support. This work was supported through grants/awards: HDTRA 135636-M, HDTRA 1410773-M, and HDTRA 1516704-M.

The Nuclear Science and Engineering Research Center at The United States Military Academy is also gratefully acknowledged for its funding and support.

Part of this work was performed under the auspices of the U.S. Department of Energy by Lawrence Livermore National Laboratory under contract DE-AC52-07NA27344.

THIS PAGE INTENTIONALLY LEFT BLANK

I. INTRODUCTION

A. SUMMARY OF WORK INCLUDED

This thesis presents three experimental efforts to optimize resonance ionization mass spectrometry (RIMS) methods on the Laser Ionization of Neutrals (LION) instrument at Lawrence Livermore National Laboratory (LLNL). The work was a collaboration between the Naval Postgraduate School (NPS) and LLNL. The goal of this work was to continue the optimization of RIMS to provide novel methods for the analysis of nuclear fallout debris and improvements in resonance ionization laser excitation schemes. The experiments were conducted to evaluate the potential use of commercial-off-the-shelf (COTS) continuous wave (CW) lasers to replace pulsed lasers currently used by the LION system, explore simplified laser excitation schemes for uranium to a one and two-color multi-photon schemes, and demonstrate sample treatment methods to improve the ability of LION to analyze actinides in nuclear fallout debris.

The chapters are arranged for sequential reading. The reader will gain the precursory knowledge necessary to understand the basic science included in RIMS in the theory chapter. Then, the process of RIMS and its components, as used in the LION instrument, are described in the method chapter. The experimentation chapter details the experiments described above. The conclusion chapter provides a summary of this work and discusses several paths forward in the development of this technology.

The remainder of this introductory chapter is meant to underscore for the reader the importance of nuclear forensics and RIMS' potential contribution to the analysis and interpretation of nuclear fallout. This chapter introduces nuclear forensics as well as describes a brief history of the development of RIMS. Understanding the strategic implications and the development history of RIMS sets the stage to understand the potential impact of LION as a method for characterizing actinide isotope ratios in nuclear materials, including nuclear fallout.

B. INTRODUCTORY VIGNETTE

Envision a birthday cake. The ingredients are predictable: eggs, flour, vegetable oil, a mix of spices, and a lot of sugar. It can be any flavor you choose.

Next, place the cake on top of a million metric tons of explosives. After detonation, the cake violently separates and mixes with the environment while in the air. Also, while airborne, it reaches temperatures well above its melting point and mixes with other molten debris. As it mixes, it falls to the earth. After the explosion has subsided, pieces of the cake are scattered in the atmosphere, on the ground, and enclosed in melted bits of the environment.

Now, envision cake forensic teams scouring the landscape taking samples. Their intent is to reconstruct the cake. They are tasked with determining the flavor, weight, and caloric content of the cake prior to detonation.

Finally, replace the idea of a cake with a nuclear weapon and you will gain insight as to the technical challenge imposed on world-class scientists who execute the nuclear forensics mission. This vignette is a helpful state of mind to understand the scope of this thesis. The work includes an immersion into the world of nuclear forensics.

C. DEFINITION OF NUCLEAR FORENSICS

A clear definition of the nuclear forensics mission is provided by *Nuclear Forensic Analysis*:

> Nuclear Forensics is the technical means by which nuclear materials, whether intercepted intact or retrieved from post-explosion debris, are characterized (as to composition, physical condition, age, provenance, history) and interpreted (as to provenance, industrial history and implications for nuclear device design). [1]

The authors of this reference provide an invaluable comprehensive introduction and source of reference material for understanding nuclear forensics investigations.

D. EXISTING PROBLEM

Nuclear forensics is a complex set of technical methods with important policy drivers and implications. The threat of a nuclear incident is no longer confined to the

Cold War model of a ballistic missile strike by an adversarial nation. The number of enemies capable of gaining access to Special Nuclear Materials (SNM) has grown to an undefined number of non-national entities and nuclear states, diversifying avenues of delivery. These two issues contribute to the likelihood that a nuclear incident may not have an immediate indicator to attribute to the hostile actor.

Nuclear forensics is the field tasked with characterizing SNM and associated materials to understand its place of origin. This thesis describes the technological method of RIMS, capable of providing isotopic ratios in material of interest in nuclear forensics investigations.

E. A BRIEF HISTORY OF RIMS

This section describes the progression of laser spectroscopy methods into the eventual realization of RIMS. The history will highlight two reoccurring themes. The first is that RIMS required the development laser technology over the course of decades. The progression of powerful and stable laser technology was directly coupled to the progression of reliable resonance ionization. The second is that the LION instrument is beginning to harness the full potential of RIMS, as expressed by past researchers. It has applied technological advancements and novel engineering to overcome the disadvantages of past system designs.

RIMS is a technology that emerged from the process of resonance ionization spectrometry (RIS), developed primarily in the United States during the 1980s. Miller [2] provides the best summary of the development of laser ablation measurement techniques and is used as the basis for the development timeline of RIMS provided in this brief history. Miller highlights the paper "Optical Micromission [sic] Stimulated by a Ruby Maser" by Breech and Cross in June 1962 as the first known publication on the ablation and excitation of atoms [3].

By the end of the 1960s, the coupling of laser ablation and "mass spectroscopy were in routine use for elemental analysis" [2]. The application of resonance excitation to isotope identification began in the sixties with the proliferation of laser technologies. Early techniques focused on spectroscopy. This meant that atoms were not excited to an

ionized state. Instead, they were excited and allowed to fluoresce (de-excite by photon emission). The experiments then measured the characteristic wavelengths of the fluoresced photons to infer elemental composition.

In the seventies, "post-excitation and post-ionization techniques were explored to analyze the neutrals ejected from the surface" [2]. The technology of identifying atoms and molecules progressed to capturing the desired species and measuring their weight-to-charge ratios after ionization (mass spectrometry). This was done by a variety of methods, the most widely used types of mass analyzers included magnetic sector, quadrupole, and time-of-flight (TOF) instruments [4].

It was not until the 1980s that RIMS technology was developed. Miller proposed that

> growth is based on two factors - the expansion and integration of laser technology into virtually every scientific laboratory and the increased number and importance of the various applications…. Concurrently, the sophistication of other laboratory equipment, particularly electronics and computers, vastly increased the experimenter's ability to acquire and analyze data. [2]

Miller creatively described laser ablation as "an answer in search of a question." As researchers used both spectroscopy and mass spectrometry on numerous elements the "characterization of large biomolecules also required increases in resolution and mass range. The use of Fourier Transform Mass Spectrometry and TOF techniques (especially reflectrons) solved these problems." The RIMS developers now had a variety of configurations and new technologies available with which to experiment [2].

Any RIMS system is defined by its three major steps. Each step can be accomplished by several methods, thus giving a wide variety of possible configurations for RIMS. The first step is atomization: creating neutral atoms in the vapor phase. During the eighties, atoms were most often atomized through evaporation using heating filaments. The second stage is resonance ionization via laser irradiation. The most commonly used laser depended on which contemporary laser technology could produce the most stable wavelength and power. The third and final stage is the detection and mass analysis of the ions produced by resonance ionization. The combination most often seen

prior to the mid-eighties was atomization by evaporation, whichever laser was the state-of-the-art technology of the time (such as a Neodymium-doped Yttrium Aluminum Garnet [Nd:YAG] or dye lasers), and mass detection by magnetic-sector or quadrupole mass spectrometers.

During the 1980s, laboratories explored different RIMS stage combinations. A team from Los Alamos National Laboratory wrote to the American Chemical Society in 1983 to say that

> Sir: Resonance ionization is rapidly being developed as a source for atomic mass spectrometric analysis. The selectivity inherent in the process can eliminate the problem of isobaric interferences, allowing the determination of accurate isotopic ratios in mixed elemental samples. [5]

The LANL team described the largest limitation of the RIMS technology as the repetition rate of pulsed lasers. They state that, "The repetition rates of commonly available laboratory laser systems fundamentally limit the fraction of the atoms in the sample that are exposed to the resonance ionization process" [5]. The limit in atoms exposed to the pulsed laser is due in great part to the continuous beam of atoms delivered by continuously heating a filament. Atoms passing through the laser beam's path while it is not irradiating cannot be ionized and are therefore lost. The author does not disclose the repetition rate of the pulsed lasers in his article [5]. Common laser technology of the era operated in the tens of hertz range.

Labs continually explored optimization techniques to increase the precision and useful-yield of RIMS. A contemporary experiment modified this technique when they "decided to pulse the atomization process by supplying current pulses to the sample filament in synchronization with the laser" [6]. The filament was pulsed 1 to 13 ms prior to the laser pulse with a width that could be varied from 3 to 9 ms. By maximizing the number of atoms delivered by the evaporation pulse into the laser beam's path, the useful-yield of measurements was increased. Useful-yield is defined by the ratio of the resonant ions detected versus the amount of the sample that is consumed during analysis.

This exploration into a pulsed filament illustrates the pursuit of optimization methods in RIMS that began in the early seventies and continues today. It also shows that

combining some steps of the RIMS process such as a pulsed laser with a heating filament are not ideal when used together. Decades of trial and error, along with the advancement of laser and computer technologies were required to advance RIMS.

John C. Miller's "Laser Ablation" was published in 1994. His historical summary ends with the following optimistic paragraph:

> All of the applications described above will certainly flourish and mature in the nineties. It remains to be seen what new applications may emerge. Or perhaps a new advance in laser technology may fundamentally change the present applications. However, the outcome, the nineties will be an exciting decade. [2]

Miller's prediction was correct. Wendt [7] describes the progression made in the decade after Miller's publication. He states that "the development of lasers as strong and quasi-monochromatic light sources with a good tunability has brought tremendous progress into various fields, among others in spectroscopy, analytical spectrochemistry, and laser mass spectroscopy." Wendt's paper argued that by the mid-2000s, RIMS was on technologically fertile ground to grow into a "competitive and/or complementary" technology [7].

It is important to make a few technological comments on Wendt's summary. First, he describes RIMS as a process in which an atomic beam source is produced from a sample that is chemically separated and then thermally evaporated. This method requires an extensive sample preparation timeline. The current state-of-the-art RIMS techniques and LION test material *in situ*, which is situated in the original place or position. Testing *in situ* samples greatly reduces the sample preparation timeline and preserves the information contained in the spatial distributions within a sample.

In his summary, Wendt lists three distinct advantages of RIMS and one disadvantage. The advantages discussed were the "almost complete suppression" of molecular and atomic isobaric interferences (the ability to differentiate atoms or molecules of the same mass; e.g., ^{238}U and ^{238}Pu), the ability to select one individual isotope for optical excitation (enabling trace detection of rare isotopes), and a high efficiency in ionization, transmission, and ion detection. These advantages are the basis

of developing the LION system for nuclear forensics. Wendt then lists his largest disadvantage: "RIMS is a strict one element technique, adaptation to a new element requires elaborate development and up to now no commercial support for routine operation is available" [7]. Figure 1 shows new data from the LION instrument conducting a multi-elemental analysis of uranium and plutonium in a mixed actinide sample, where both elements are measured simultaneously from the same volume. LION is the instrument that John Miller optimistically predicted.

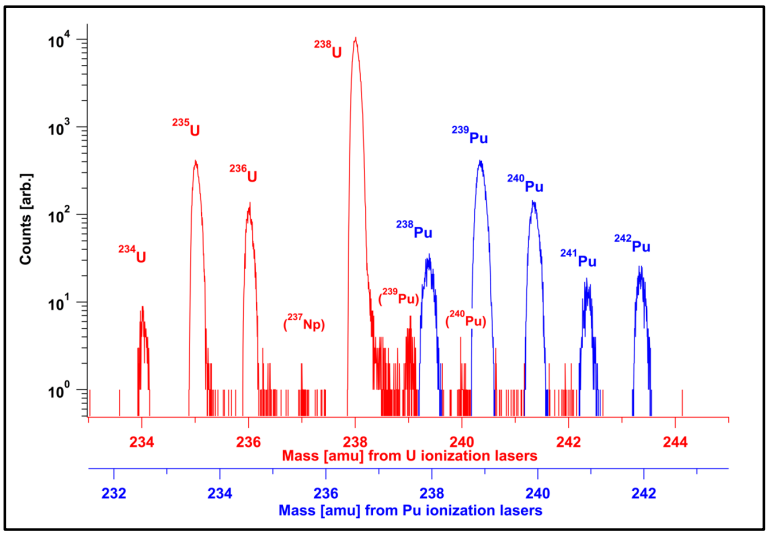

Figure 1. RIMS measurement of uranium and plutonium isotope ratios simultaneously on the LION Instrument at LLNL. Source: [8].

After nearly forty years of development, RIMS is in the proof-of-concept phase, represented by LION, to become a robust system for characterizing actinide isotope ratios in a variety of nuclear materials. LION is the culmination of years of optimizing processes and procedures to eject neutral atoms into the path of reliable laser beams for high ionization efficiency prior to entering a high transmission time-of-flight mass spectrometry (TOF-MS) system. LION began operation in October 2015 at LLNL. This thesis describes a set of current research activities serving to optimize RIMS and advance the applicability of LION as a technique to a variety of applications including safeguards, non-proliferation, and nuclear forensics.

THIS PAGE INTENTIONALLY LEFT BLANK

II. THEORY

A familiarity with three processes is required to understand the scope of this thesis. Information included here is presented at a level below that of a subject matter expert but above a cursory knowledge. The first topic covered is laser resonance ionization. Two of the three experimental efforts in this work deal exclusively with resonance ionization. It is also the most specialized and important step in RIMS. Next is an overview of nuclear debris formation. The formation overview will develop the reader's knowledge of how a sample may be formed in the aftermath of a nuclear detonation. Finally, the atomization step is discussed in this chapter. The atomization step removes material from the surface of the sample during measurement to produce a neutral cloud of atoms in the vapor phase. The LION system can use ion sputtering or laser heating to atomize samples. The understanding of the atomization process becomes important during the experimental investigation of actual fallout debris.

A. LASER RESONANCE IONIZATION

Laser resonance ionization is the method of exciting atomic electrons to states with a high probability of ionizing; creating an ion and a free electron. As mentioned in the previous discussion of the history and development of RIMS, knowledge of resonance ionization comes from spectroscopic methods and reaps the benefits of decades of research and practiced methodology. This section develops the readers' understanding from the quantum mechanical definition of an electron orbit and leads to the understanding of easily photo-ionized states.

1. Rate Equations

The quantum mechanical process of transitioning from one state to another in the presence of a radiation field was first described a century ago. In 1917, Albert Einstein's article, "On the Quantum Theory of Radiation" [9], discussed the conservation of momentum under the conditions of the absorption and emission of radiation. In a section named "Hypotheses on the radiative exchange of energy," Einstein laid the theoretical foundation for stimulated absorption and emission by a molecule or atom. His

assumptions and flawlessly simple conceptualization later led to the technological revolution of the laser.

He states that in a two-state quantum mechanical system, which we will define as state 1 and state 2, "an oscillating Planck resonator radiates energy in the well-known way." He quantifies this "well-known way" with an equation for the probability of the transition from state 2 to state 1.

$$dW = A_{21}dt \tag{2.1}$$

where *dW* is the probability of a transition occurring during time interval *dt* and A_{21} "is a constant characterizing the index of combination" from state 2 to state 1. When multiplying the probability of a transition by the number of atoms or molecules populating state 2, N_2, and dividing by *dt*, Equation 2.1 becomes the rate of transition due to spontaneous emission from state 2 to state 1 as shown in Equation 2.2. dN_2/dt is the change in the population of state 2 over a time interval *dt*. A transition that increases the population in the state is represented by a positive term and a negative term represents a term that decreases the population.

$$\frac{dN_2}{dt} = -A_{21}N_2 \tag{2.2}$$

Einstein states that under the influence of a radiation density ρ the probability of a transition from a lower state, 1, to a higher state in energy, 2, in a two-state system is defined by Equation 2.3. Here he argues that the probability of a transition as a function of time is proportional to the radiation density of the irradiating light. The constant B_{12} is the likelihood of an optical excitation, from the laser providing radiance density, ρ, causing a transition from state 1 to state 2.

$$dW = B_{12}\,\rho\,dt \tag{2.3}$$

Similarly, he argues that the transition "associated with a liberation of radiation energy" from the higher state, 2, to the lower state, 1, is defined by Equation 2.4

$$dW = B_{21}\,\rho\,dt \tag{2.4}$$

He gives these processes the name "changes of state due to irradiation" [9]. Multiplying Equation 2.3 and 2.4 by the population of the state supplying the transition and dividing by *dt* results in the rate equations for stimulated absorption and emission

shown in Equations 2.5 and 2.6. These terms are negative because they cause a decrease in the population of their respective state.

$$\frac{dN_1}{dt} = -B_{12}\,\rho\,N_1 \tag{2.5}$$

$$\frac{dN_2}{dt} = -B_{21}\,\rho\,N_2 \tag{2.6}$$

Analyzing these equations shows that a radiation density, ρ, will cause both stimulated absorption and stimulated emission in a two-state system. The rate equations and transitions are shown in a vector representation for a two-state system in Figure 2. In Figure 2, the green line pointing upward represents stimulated excitation (absorption of a photon), the first red line pointing downward represents stimulated emission (release of a photon), and the second red line represents spontaneous decay (release of a photon). If the rate of stimulated excitation is greater than the rate of stimulated emission and spontaneous decay, there will be more atoms in state 2 than state 1 once the system comes to an equilibrium point after a period of time. RIMS uses this process to populate excited states with a high probability of creating an ion and free electron.

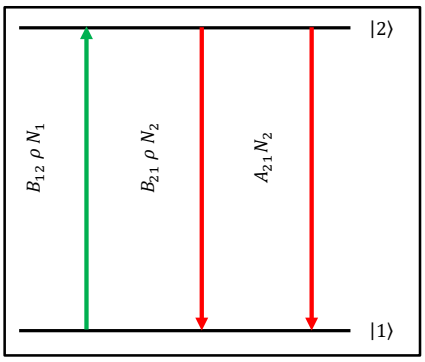

Figure 2. The rate equations illustrated as vectors for a two-state quantum mechanical oscillator located in a radiation field.

2. The Time-Dependent Schrödinger Equation

This derivation explains why excited states have a bandwidth, instead of a finite, energy associated with the state. Similar derivations can be found in any number of quantum mechanics textbooks. The logic used here is like that of Letokhov [10].

The states of a quantum mechanical oscillator are not defined exactly. The states have an uncertainty in energy due to the process of spontaneous emission. A mathematical explanation is required to define the uncertainty, or bandwidth, in each state. The Time-Dependent Schrödinger Equation of a system is defined by Equation 2.7.

$$\Psi(t) = \Psi_o e^{\frac{-iE}{\hbar}t} \tag{2.7}$$

If Equation 2.7 defines the excited state of an atomic electron, we know that over time, it will decay. Therefore, it should normalize to Equation 2.8.

$$\langle \Psi | \Psi \rangle = e^{-\lambda t} \tag{2.8}$$

Lambda, λ, is described as the frequency of spontaneous decay. If there are multiple decay channels lambda is the summation of the frequency among all decay channels, $\lambda_m = \sum_n \lambda_{mn}$. Where m is the state being described and n is any allowable decay destination.

For the Time-Dependent Schrödinger equation to normalize to Equation 2.8, the energy must be imaginary. We can define the energy to have an imaginary portion. $E = E_o + i\gamma$. Replacing the imaginary energy into Equation 2.7 and normalizing will show that λ must equal -2$\gamma/\hbar$.

This result requires exploration. Since λ is the frequency of decay, its inverse is the decay time constant τ. Invoking the Heisenberg Uncertainty Principle, Equation 2.9 relates the uncertainty in the lifetime of the state to the uncertainty in the energy of the state.

$$\Delta E \Delta t \approx \hbar \tag{2.9}$$

If the uncertainty in the lifetime of the state is $\Delta t = \tau$, then the uncertainty in energy is defined as

$$\Delta E \approx \hbar/\tau \tag{2.10}$$

Here, we can redefine ΔE for our own purposes. We will define it as Γ. Γ is defined as the full width at half measure of energy allowed in the excited state. Using our definition of Γ, we can rewrite γ as $-\Gamma/2$. Rewriting the Equation 2.7 with Γ results in Equation 2.11. Figure 3 shows a simple two-state quantum mechanical oscillator and the width, Γ, of the excited state. This result shows that optical excitation is possible with high probability over a bandwidth of frequencies defined by Γ.

$$\Psi(t) = \Psi_o \, e^{-\frac{i}{\hbar}(E_o - \frac{i\Gamma}{2})t} \tag{2.11}$$

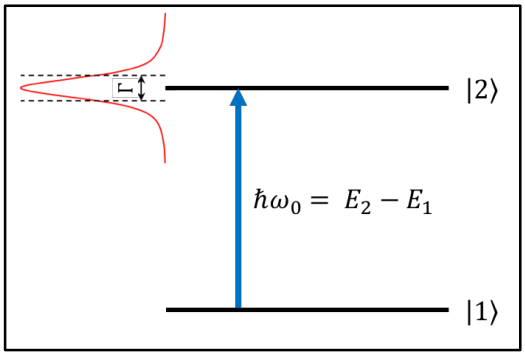

Figure 3. Two state atomic model with excited state bandwidth of Γ.

3. Stimulated Excitation to Bound States

Photons of the correct frequency can excite electrons from one state to another. The frequency must be tuned such that the energy of a photon, or multiple photons, equals the energy difference between the two states, within Γ, as shown in Figure 3.

The transition depends on the interaction between the photon and the atom. In the presence of many coherent photons, the interaction may be modeled as electrons interacting with an electric field. The interaction is modeled as the dipole moment of the atom with the electric field. The dipole moment is defined by Equation 2.12,

$$\hat{\mu} = e \sum_i \hat{r}_i \tag{2.12}$$

where *e* is the charge of an electron and r is the radial vector of the i^{th} electron in a multi-electron atom. For our purposes, we will not develop the atomic dipole moment further. It is only important to understand that the monochromatic laser light is modeled as an electric field that interacts with the dipole moment of an atom.

As the laser power increases, the density of photons reaches a value that makes the electric field model of a laser valid. The amplitude of the field interacts with the dipole moment of the atom. This interaction raises and lowers the energy of the atoms valence electrons. If the field's energy is within Γ of an allowed excited state, the valence electron will undergo a transition with high probability. Reaching a photon density to ensure that all atoms within the laser beam's irradiation have a high probability of transition is referred to as saturation. An individual atom may undergo multiple transitions, both upward and downward, due to the electric field produced by a laser with a power capable of saturation. The frequency that the atom transitions back and forth in a quantum mechanical oscillator is known as the Rabi frequency.

4. Ionization Processes

The final step of resonance ionization is to ionize the target atoms. This section discusses the final transition of electrons into easily ionized states. The three ionization states used in resonance ionization are shown in Figure 4. Figure 4 uses slightly different terminology than what is commonly used in RIMS research. The most important difference in terminology is that the ionization limit is referred to as the ionization potential (IP) in this thesis. This section discusses ionization into the continuum, auto-ionizing (AI) states, and Rydberg States to explain how resonance ionization creates ion and free electron pairs.

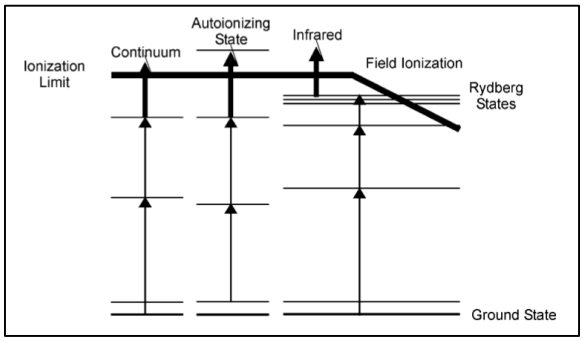

Figure 4. A depiction of the three ionization processes used in resonance ionization. Source: [7].

The first process discussed is excitation into the continuum, meaning that the density of states above the ionization potential is so high that one cannot always identify a specific quantized state. Previous researchers have quantified the structure of the continuum of states that exist above the IP for uranium. One such study is included in [7] and is summarized in Figure 5. The energy units shown on the graph are in wave number: a spectroscopy unit of wavelength expressed in inverse centimeters. The IP energy begins on the left side of the figure; 49958.4 cm^{-1}. Moving right on the graph indicates an increase in energy above the IP.

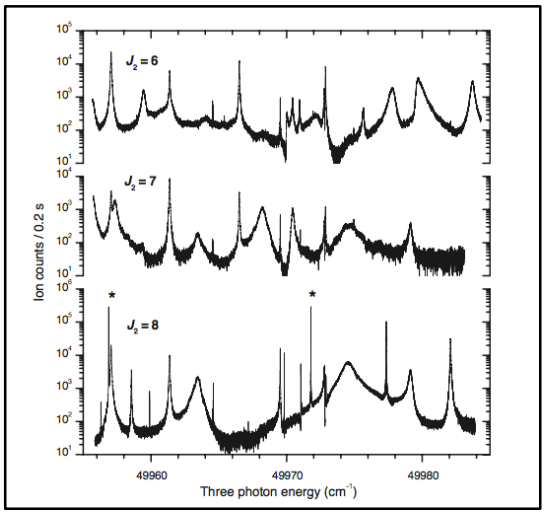

Figure 5. Spectra of excitation above the ionization potential for ^{238}U from different intermediate states with different angular momentum, $J = 6,7,8$. Source: [11].

The key point from this graph is that spectroscopy research has quantified the ionization probabilities for energies above the IP for uranium for multiple values of *J*, the total angular momentum. It is important to understand that exciting uranium above the IP does not result in a uniform ionization probability. Many factors govern the relative ionization probability in the continuum. Depending on the total angular momentum of the excited state prior to excitation above the IP, uranium has varying ionization probabilities. This phenomenon is why Figure 5 has three separate graphs. It is comparing the ionization potential of uranium originating from various excited states with different total angular momentum values, J = 6,7,8.

Resonance ionization schemes can use studies and graphs such as Figure 5 to target specific final ionization transitions from excited states with known *J* values. Later, a suggestion for continued research for the one- and two-color uranium resonance ionization schemes will refer to this method of scanning the continuum as an area for future research.

The shape of the graphs in Figure 5 are important in understanding relative ionization probabilities for different ionization schemes of uranium. There are structures, in the graphs shown in Figure 5, which are best described as valleys and peaks. The valleys are a super-position of the edges, or tails, of the probability distribution of many states. This superposition of many states results in a continuum of states. Excitation into the continuum, but not into a well-defined state often results in a low ionization probability. There are regions of the continuum with relatively high ionization rates with broad widths. Figure 5 has two such regions in the J=8 spectrum at 49964 cm^{-1} and 49975 cm^{-1}.

The peaks represent the second ionization process; AI states. AI states are well-defined states above the IP with a high probability of ionizing. An AI state is described by the excitation of the inner shells of an atom. When the cumulative excitation energy of multiple electrons is above the IP of the atom, it is highly likely that the atom will relax by transferring the energy to a single valence electron. This single electron with excitation energy above the IP has a high probability producing an ion and a free electron. Figure 5 shows that transitioning to an AI state is one to two orders of

magnitude more likely to cause an ion and free electron than transitioning into the continuum.

The final ionization state to discuss is the excitation to a Rydberg state. A Rydberg state is a highly-excited atom at an energy just below its IP. These states are easily ionized through the application of an electric field, collisions with other atoms, or further optical excitation [10]. The ionization of an atom by an external field is possible due to the Stark Shift which lowers the relative IP in the presence of a strong field. This process is postulated to be the reason why a portion of the two-color uranium scheme, to be discussed in the experimentation chapter, creates an ionization signal even though it does not provide sufficient energy to excite an electron above the IP.

In summary, there are three ionization states used in RIMS. These three states were excitation into the continuum, AI states, and Rydberg states. Together these three states describe the final states of the optic excitation in resonance ionization that lead to the creation of an ion and a free electron.

B. NUCLEAR FALLOUT DEBRIS FORMATION

Nuclear debris comes in two major forms: aerodynamic and non-aerodynamic. Non-aerodynamic are samples that may have been embedded in an object during the initial blast. A portion of this research focuses on aerodynamic samples. L.A. Lewis describes aerodynamic fallout in the following excerpt:

> Glassy fallout forms when a nuclear device is detonated on or near the Earth's surface. Surface detonations melt large masses of environmental material (e.g., soil), which may remain in place or be swept into the nuclear fireball. In both cases, the molten material may interact with device components, fission and activation products, and unfissioned fuel. As the fireball cools below the melting point of the surrounding material, device debris becomes trapped within a fused glassy matrix and rapidly cools, forming glassy fallout. Because the mass of melted environmental material can be much greater than the mass of the device near the surface events, the major element compositions of these glasses can predominantly reflect the local geology and/or emplacement environment, and device debris is generally present only in trace quantities (Adams and O'Connor, 1957; Miller, 1964). [12]

With this description, many assumptions can be made. First, debris will undergo thermal diffusion throughout flight. The diffusion consists of refractory (high-melting temperature) and volatile (low vaporization temperature) species. Elements will be continually collected on the surface and mix into the sub-surface region of a sample. Second, the debris may collide with other molten debris forming irregular shapes. Figure 6 shows a model for fallout debris formation.

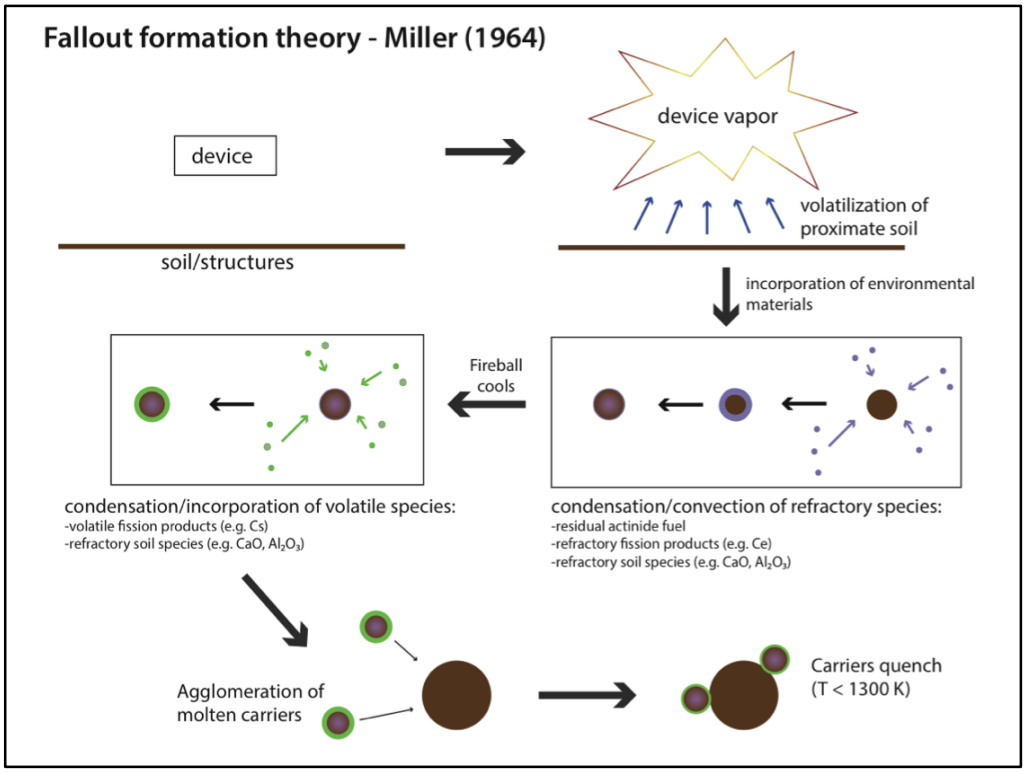

Figure 6. Fallout formation model. Source: [13].

Fallout debris samples will have different mixes of device components and local geology at different concentrations depending on its interaction with the nuclear fireball. Early fallout studies primarily collected fallout debris for the study of possible health concerns in downwind areas due to testing at the Nevada Test Site. Figure 7 shows a recording of fallout particles collected from a test at the Nevada Test Site. This unclassified report shows the categorization of numerous fallout samples by size, color, shape, opaqueness. The diversity in samples shows the challenge that is entailed in the

surface sampling of nuclear fallout debris. The samples will consist of mainly silicate materials, but the surfaces may vary widely in elemental and isotopic compositions.

Table A.1--PRELIMINARY CHARACTERIZATION OF SHOT PRISCILLA RADIOACTIVE FALLOUT PARTICLES COLLECTED 7000 YARDS FROM SURFACE ZERO

Particle No.	Size in microns Max.dia.	Min.dia.	Relative gamma activity at H+340 hrs, counts/min	General shape	Color	Remarks
20-A-A	3115	930	11,800	Cylindrical	Opaque, yellow brown	Glassy, opaque with melted bubbly surface projections
20-A-B	1810	1020	430	Bean-like	Cream opaque	Glassy smooth surface with cracks, particle broken, surface appeared melted
20-A-C	2560	2560	3,066	Disc with jagged edges	Opaque, rose grey	Rough disk shape, small bubble on surface may indicate partial melting
20-A-D	1440	1440	24,626	Spherical	Transparent with black specks	Glassy, many small spheres or bubbles on surface, melted
20-A-E	2880	1900	10,650	Rough ellipsoidal	Sand, semi-transparent	Melted surface with glassy bubbly appearance in spots, unmelted interior contains black specks
20-A-F	2320	2090	9,318	Angular	White, semi-transparent	Quartzlike, jagged edges, however, smooth melted surface
20-A-G	1160	1160	1,347	Spherical	Cream, semi-transparent	Melted slightly bubbly appearing surface, grey green inside
20-A-H	2930	2100	25,894	Angular irregular	Sand opaque	Melted, bubbly projections on surface
20-A-I	1395	1350	3,575	Spherical	White, semi-transparent	Melted, internal bubbles
20-B-A	980	980	35,592	Spherical	Transparent, olive green	Nearly perfect sphere, smooth surface interior has bubbles and black specky material
20-B-B	2140	1630	Not counted	Angular	Sand opaque	Very slight indication of partial melting on surface, weak autoradiograph
20-B-C	1720	1580	Not counted	Angular	Cream sand opaque	No indication of melted surface, very weak autoradiograph

Figure 7. Categorization of fallout samples by size, gamma activity, shape, and color from Operation Plumbbob. Source: [14].

M.A. Fitzgerald summarized the composition with historical studies included to draw important conclusions:

> The melted soil is the source of the macro-scale carrier material that transports vaporized bomb, anthropogenic, and environmental material from the fireball into the local environment as fallout…. Historical studies suggest that the vaporized mass contribution to the melt is minor; in a surface-burst, approximately 5000 tons of soil are displaced per kiloton yield, but only 25 tons are vaporized (Izrael et al., 1970). The duration of heating is brief, on the order of seconds (Cassata et al., 2014), which presents little time for chemical fractionation to occur. Weisz et al. (2016) observed an enrichment of condensate along the exterior of similar

objects, a pattern consistent with such glasses interacting with, but not forming from, a condensate. [15]

These insights refine our understanding of the formation of fallout following a nuclear detonation. First, environmental materials are pulled into the plume and heated to cause at least the surface layers to melt. Shortly, on the order of seconds after detonation, the bulk material begins to cool. The fallout debris collects both refractory and volatile species onto its surface and especially into boundary regions of inclusions. The results are aerodynamic glassy materials with bulk compositions representative of a mixture of the environmental material and the device.

Weisz [13] studied fallout formation and the boundary composition between fallout and aerodynamic inclusions. A few important theories are developed in this work. First, the mixing process appears continuous for both refractory and volatile species. The study of some boundary compositions showed both refractory (Fe, Ca, Mg, Mn, and U) and volatile (Na) species. Second, the boundary regions often showed a lack of Al, which is abundant in the soil, but an enrichment in ^{235}U and Fe. This is evidence of "an anthropogenic source of the enriched species or an unexpected vaporization/condensation behavior" [13].

Figure 8 shows a nuclear fallout debris sample. The debris appears aerodynamic and glassy with two major inclusions. This sample was received from Weisz [13] and is used in testing described in the experimental chapter.

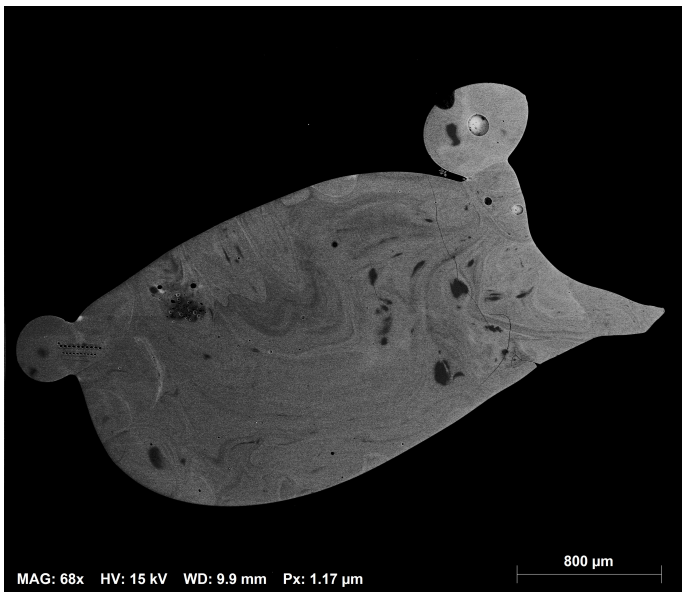

Figure 8. Nuclear fallout debris under scanning electron microscope (SEM). Sample is polished to the mid-plain and embedded in epoxy. Actual sample obtained from Weisz [12].

C. ATOMIZATION OF MATERIAL

The LION instrument has two available means for atomization of the surface of a sample: laser ablation and ion sputtering. The characteristics of both processes are discussed in this section.

1. Laser Ablation

The main process of laser ablation is the excitation of electrons in the target which then cause motion in the material. Miller [2] stated that "initial electronic excitation is converted into the driving energy for nuclear motion, resulting in the ejection of atoms, ions and molecules from the surface." He also states that the interaction depends on the electron-lattice interactions, which depend on the characteristics of the solid. This explanation begins to indicate why different materials interact differently with the same ablation laser.

Laser ablation has three primary benefits over its main alternative ion sputtering. The first is that the surface does not need to be electrically conductive. The second is that it removes more material than ion sputtering. The ability to remove more material makes

it better suited for samples with lower uranium and plutonium concentrations. Finally, the velocity distribution of the ablated atoms is lower with laser ablation than with ion sputtering. Laser ablation causes a smaller uncertainty in the time-of-flight (TOF) for atoms of the same mass than sputtering, an important consideration for the TOF mass spectrometry that is an essential part of the LION-RIMS process. Ion sputtering is described later in this chapter.

To understand the laser ablation of nuclear fallout debris it is helpful to think about the solid-state physics and the characteristics of silicon dioxide (SiO_2) as a simplified representation of the bulk composition of glassy aerodynamic fallout. The following sub-sections describe the characteristics of SiO_2 and the quantum mechanical process of thermal ablation. While actual fallout consists mostly of SiO_2, the mixing of impurities into the matrix causes variation from the material characteristics of pure SiO_2. This simplification offers a basis for making theoretical perturbations.

a. Solid-State Physics and Silicon Dioxide

A brief development of solid-state physics is required to understand the difficulty in using a laser to ablate SiO_2. SiO_2 is one of the most common molecules on earth. It is sand. When fused together in a solid-state, it forms the molecule as shown in Figure 9.

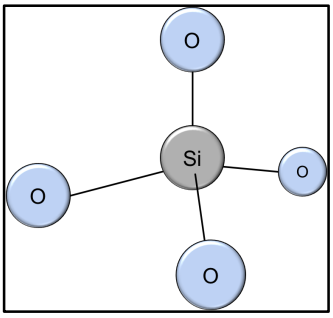

Figure 9. 2D representation of SiO_2 forming the SiO_4 tetrahedron in its solid-state form.

Nuclear fallout debris consists of amorphous-SiO_2 (a-SiO_2) as the bulk material as discussed previously. A diagram of an a-SiO_2 structure is shown in Figure 10. The term

"amorphous" means that the material does not follow a uniform crystalline pattern. The structure does not keep the same pattern or structure over the entire extent of the sample. The lack of uniformity in the structure means that the bonding energy between any two molecules or atoms is not uniform throughout the structure. It also means the bonding energy of electrons is not uniform. This has many implications for optical excitation. The computer-chip industry uses a-SiO_2 for its insulating properties. Insulating materials do not have electrons in a conducting band. This is due to a large energy bandgap between the valence and conducting bands. The implications of this are discussed in the next section.

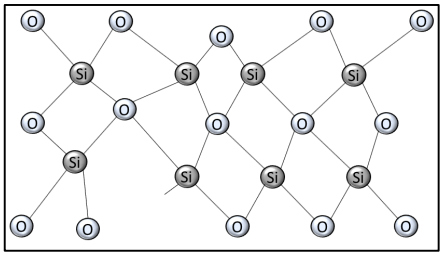

Figure 10. A 2D representation of an a-SiO_2 structure.

b. Thermal Ablation

Electric fields produce heat by exciting electrons. The motion of the electrons causes motion of nuclei. As atoms reach kinetic energies above their binding energies, they can be expelled from their solid-state structure. This is the basis for thermal ablation.

Solid-state materials are held together by valence electron bonds. With sufficient temperature ($kT \geq$ band-gap energy; where k is Boltzmann's constant and T is temperature), electrons will be thermally excited into a conduction band. Figure 11 shows a diagram of the valence and conduction bands.

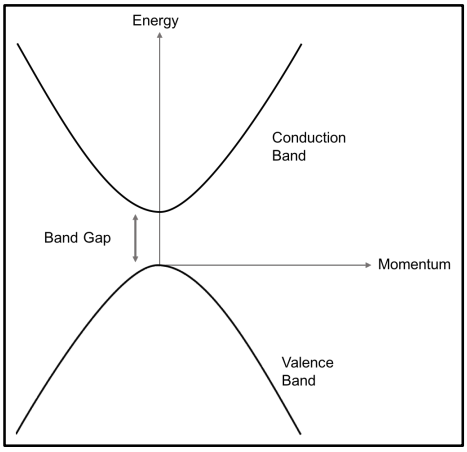

Figure 11. Plot of valence and conduction bands on energy versus momentum graph.

A single photon with an energy less than the band-gap energy ($h\nu$ < band-gap) will not interact with the material. Multiple photon absorptions can cause excitation across the band-gap. The probability of this type of excitation decreases with each additional photon required. A material that does not interact with a certain wavelength of light is referred to as transparent at that wavelength. A photon, or multiple photons, with energy greater than the band-gap energy ($h\nu \geq$ band-gap energy) of a material can optically excite electrons from the valence band to the conduction band. The excitation of an electron from the valence band also creates a "hole" in the valence band. The electron and hole pair both cause motion in the bulk material. This motion creates heat in the material. Figure 12 shows the process of optical excitation from the valence to the conduction band (red). Both the electron and hole will interact with the bulk material until the electron occupies a state with the lowest possible energy (green). The electrons in the valence band will also reposition until the hole occupies the state with the highest energy. These processes cause an increase in the average kinetic energy of the material and an increase in temperature.

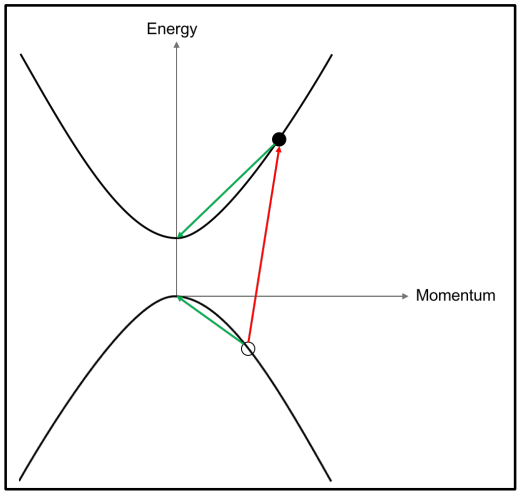

Figure 12. Electron-hole excitation and interaction process depicted on an energy-versus-momentum graph.

A photon from a laser can optically excite a valence electron to the conduction band. The larger the band gap between the valence and conducting band, the smaller the wavelength required to optically excite an electron. A thin material can be illuminated to measure the band-gap. Figure 13 shows the transmission of light in a-SiO_2 versus wavelength for multiple thicknesses from [16]. This study measured the band-gap of a-SiO_2 to be approximately 9.3 eV or the energy of a 133 nm photon. The material appears transparent to wavelengths longer than this wavelength. As the photon reaches sufficient energy to cause an electron to excite across the band-gap from the valence to conduction band, the material becomes less transparent. A sufficiently thick material appears opaque to photons with energies higher than the band-gap.

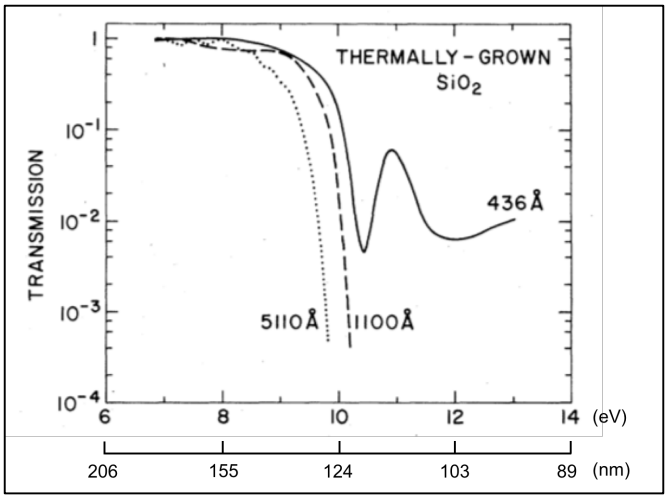

Figure 13. Plot of the energy of light versus transmission in amorphous-silicon dioxide substrates with thicknesses of 436, 1100, and 5110 angstroms. Original x-axis in eV, author placed second x-axis in nm. Source: [16].

The ablation lasers currently used with LION, described in the method chapter, produce photons of 1 to 3 eV. At these energies, accounting for both single photon and two-photon interactions, a-SiO_2 is transparent. Unless a sample has numerous defect spots that cause a smaller band-gap or was treated with an opaque material, the lasers would not efficiently transfer energy into the sample.

The transfer of energy to the sample is required for thermal ablation. The likelihood of the material ejecting particles increases with the heat absorbed. Particles with increased kinetic energy can break bonds with the bulk material. Each material has different characteristics under thermal ablation. As the material heats it reaches a melting point. The ejection of particles becomes more likely after the region of the particle reaches the melting point of the material. If a material diffuses heat at a high rate or has a higher melting temperature, it will take more irradiation to heat a given volume.

2. Ion Sputtering

Ion sputtering uses accelerated ions to impart kinetic energy into the solid-state material. Reference [17] describes the process as "a physical or chemical change: radiation damage and/or defect formation, sputtering on the target surface, and a general increase in the target temperature." Reference [18] further explains that, "by penetrating

into the crystal the primary ion suffers collisions with the lattice atoms located in the first atomic layers and sets them into motion. In turn, these atoms initiate collisions cascades, which can end up by the ejection of several particles. This is the sputtering phenomenon."

A model of sputtering is presented in Equation 2.13 [18]. This equation gives an understanding of the sputtering yield, S_o, due to ion bombardment of a surface.

$$S_o = 0.042\text{Å}\ \alpha\left(\frac{M_2}{M_1}\right)\frac{Sn(E_o)}{U} \tag{2.13}$$

In Equation 2.13, M_1 is the ion mass, M_2 is the impacted atom mass, $Sn(E_o)$ is the stopping cross section of the incident particle in the solid, U is the binding energy, and $\alpha\left(\frac{M_2}{M_1}\right)$ is a constant calculated according to the ratio of the masses. This equation describes the sputtering yield as directly proportional to the ratio of the energy of the bombarding ion versus the binding energy of the material. Equation 2.13 is calculated for a normal (90 degree) incidence, though the angle of incidence does affect the sputtering yield. For low energy bombardment (~ 1 keV) the dependence on the angle of incidence is shown in Equation 2.14 [18].

$$S(\theta_i) = S_o\ |\cos\theta_i|^{-1} \tag{2.14}$$

In his lengthy development of ion beam science, Sigmund [19] provides a simplistic example of ion sputtering shown in Figure 14. The ion impacting the surface undergoes several elastic collisions transferring kinetic energy each time. The atoms impacted by the ion may impact other atoms. One collision can cascade into multiple collisions and ejected atoms. This is what is meant by sputtering yield: on average, the number of atoms ejected per primary ion impacting the surface.

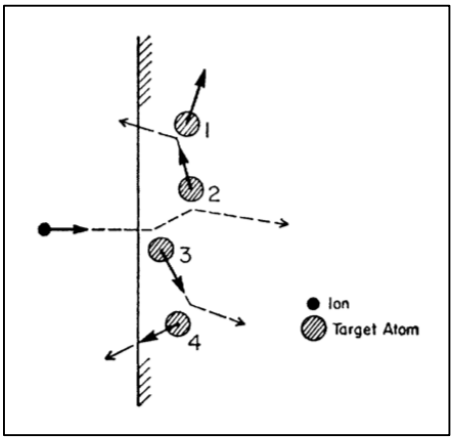

Figure 14. Simplified diagram of ion sputtering. Source: [19].

The cascade effect of sputtering causes a larger velocity distribution than in the case of laser ablation. Prior work by the LION team assumes that the velocity distribution follows a Maxwell-Boltzmann distribution [20]. The Maxwell-Boltzmann distribution is described by Equation 2.15.

$$\frac{dN}{N} = \sqrt{\frac{m}{2\pi kT}} e^{\frac{-mv^2}{2kT}} dv \tag{2.15}$$

where dN/N is the fraction of molecules moving between v and $v + dv$, m is the mass of the atom, k is the Boltzmann constant, and T is the temperature. This distribution describes the probability of finding a particle at a given velocity.

A larger velocity distribution causes a larger dispersion of kinetic energies of the particles in the ablated cloud. A larger distribution of kinetic energy means that particles of the same mass will have a distribution in velocity as they travel to the detector. This causes the mass peaks to widen in a mass spectrum. This process is discussed further in the method chapter in the mass analysis and ion detection section.

III. METHOD

This chapter summarizes the technical knowledge necessary to understand the method of RIMS as executed by the LION instrument. The reader needs to know the three steps of RIMS; atomization, resonance ionization, and mass analysis and ion detection. This chapter is organized to explain those three steps in sequence as executed by LION.

A. STEP ONE—ATOMIZATION

The atomization step consists of sample preparation, placement in the instrument, and the production of a neutral cloud of atoms above the target surface. All of the samples tested by LION are solids. Chemical purification is not required for a RIMS measurement; this allows for *in situ* testing. Prior to atomization, the sample must be mounted on a sample pedestal and placed within the instrument in the correct position for testing. Commonly, samples are either pressed into a soft metal, such as indium, embedded into epoxy, or simply taped to a target pedestal. Figure 15 shows fragments of a sample crushed and pressed into indium.

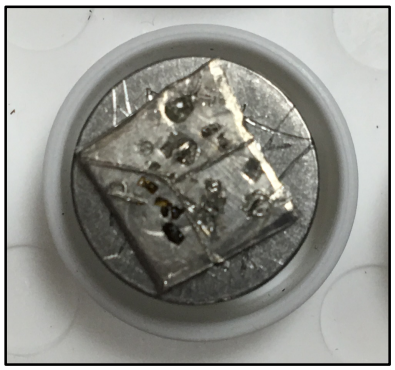

Figure 15. Sample crushed and pressed into iridium on a half-inch target pedestal.

Uranium standards are used to provide samples of known isotopic composition for the purpose of quantifying the measured performance of the RIMS process. Figure 16 shows a certified uranium standard CRM125A situated in the target chamber of LION.

This uranium standard is uranium oxide immobilized with doubled sided tape. These samples are often coated with a layer of carbon to prevent charging of the sample surface during electron or ion bombardment.

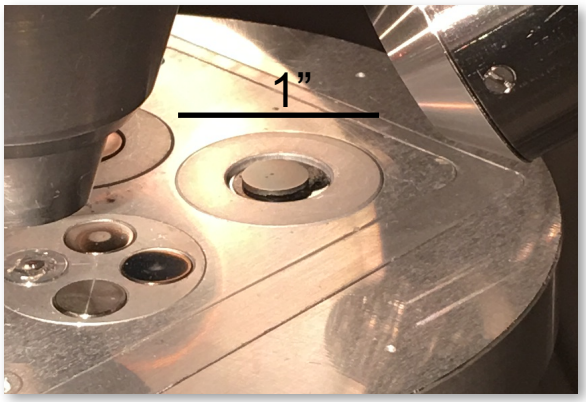

Figure 16. Uranium-oxide standard, sample CRM125A, immobilized on carbon double-sided tape on an aluminum pedestal. The sample is shown in the target chamber of LION.

Target pedestals holding immobilized samples are placed in one of up to sixteen known positions contained in the target stage. The target stage is responsible for ensuring the correct positioning of the sample. The laser ablation, or ion sputtering, beam and resonance ionization laser beams are set to intersect at a pre-determined position within the target chamber. This pre-determined point ensures that the atomized cloud is positioned for subsequent irradiation by the resonance ionization lasers. The target pedestal can move in all three dimensions to ensure that the sample surface is correctly positioned in the target chamber. Figure 17 shows the inside of the target chamber while a measurement is being made in the LION instrument. The purple light is due to the light introduced by the resonance ionization lasers.

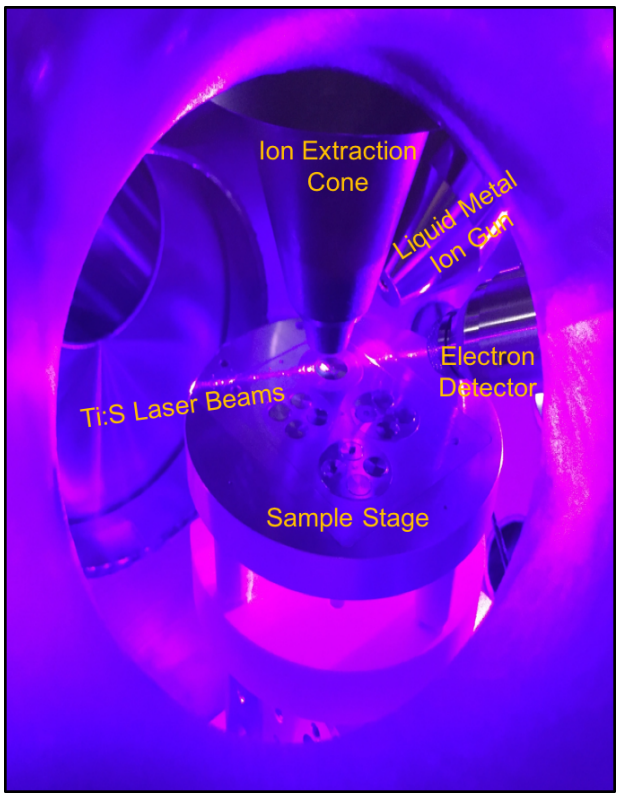

Figure 17. LION instrument target chamber during operation. Labeling added. Source: [20].

The first method of atomization available is laser ablation. This is the process of exposing a portion the target surface to an intense photon field. The desired effect of exposure is the ablation of a portion of the surface without forming a plasma above the sample. As discussed in the theory chapter, the experimental effect depends on the surface characteristics. A surface that is transparent to the applied laser wavelength will not ablate well. This can be a problem with silicate-matrixes, such as fallout debris. The other defining characteristics include how well the surface diffuses heat throughout the bulk material and its melting point.

Several different laser ablation methods are available and can be used depending on sample characteristics. The LION instrument uses either a Nd:YAG laser tripled to 351 nm with a pulse length of 25 ns or a femto-second laser at 800 nm with an approximate pulse length of 140 fs. The femto-second laser can be extended to a nano-

second pulse length (~10 ns) at the same 800 nm by blocking a component. Also available is a Nd:YAG laser at 1064 nm with approximately 5 ns pulse lengths.

The second method of atomization is ion sputtering. Two means of sputtering are currently available to LION. The first is a liquid metal ion gun. The an *Ionoptika* IOG-25 ion gun which can accelerate Gallium or Gold ions to 10–25 keV with beam currents of up to 10 nA, although typical analyses require tens to hundreds of picoamps of beam current. The second is a *Hiden* Analytical IG20 gas gun that can provide a wide range of ions from a variety of gases including hydrogen, argon, neon, and methane for example. The IG20 gas gun can deliver ions with energies up to 5 keV to a circular spot size with a diameter of 100 microns. The impact of the ion beams provided by these guns results in inelastic collisions with the surface. Upon collision, the ion imparts energy into the target, which results in kinetic energy larger than the target's binding energy. The target may also begin a cascading collision with neighboring particles. Several particles can be ejected. The ejected particles can be atoms or molecules, neutral or ions.

The specifics of the ion sputtering method are as follows. The LION system commonly uses a spot size of approximately 1 μm^2. This beam spot can then be rastered. This means the spot scans over a surface, commonly a 10 μm x 10 μm area or larger. Each pulse of the ion beam commonly lasts for 300 ns, but the pulsed time can vary from 50 ns to a continuous beam.

The final process in producing a neutral cloud of atoms is the removal of any ions created during the atomization step. These ions are referred to as secondary ions. The percentage of secondary ions versus secondary neutral species ejected from surface is measured as low as 1%. [21] These secondary ions are the same ions used in the method called secondary ion mass spectrometry (SIMS). In the method of RIMS, these ions are typically discarded by pulsing a strong electric field prior to the irradiance of the resonance ionization lasers. The strong electric field cause the secondary ions to be ejected from the back of the reflectron (discussed in Step Three – Mass analysis and Ion Detection). After the ejection of the secondary ions, then the resonance ionization step occurs (discussed in Step Two – Resonance Ionization). The resonantly-created ions are extracted by a second electric field pulse after the irradiance of the resonance ionization

lasers and allowed to travel to the detector. The resonantly-created ions are not ejected from the reflectron and are collected for analysis.

B. STEP TWO—RESONANCE IONIZATION

The most defining step of RIMS is laser resonance ionization. The theory of resonance ionization was discussed previously in the theory section. This section discusses the application of the lasers to selectively ionize the desired element in the atomized sample.

After the secondary ion ejection, the cloud consists of neutral atoms and molecules. A number of lasers then provide photons capable of selectively exciting the atoms of the desired element in the neutral cloud in a multi-step excitation process leading to ionization. The LION uses multiple Ti:Saph lasers with fundamental wavelengths tunable between 700–1000 nm. The lasers can be frequency doubled to provide wavelengths between 350–500 nm and tripled to provide 125–250 nm.

The LION system is currently equipped with six Ti:Saph cavities. Each laser, while in operation, is automated to ensure the mean wavelength does not drift. The timing of each pulse is also automated by triggering a Pockel's cell[1] with a delay generator, in order to reproducibly trigger a laser cavity relative to the overall system timing to within 1–2 ns. Currently, the precise timing of each laser with respect to the other lasers used for ionization is manually adjusted. This requires periodic checking of the relative timing between lasers.

An example of a 3-color uranium excitation scheme is shown in Figure 18. The Ti:Saph lasers are tuned to 415.5105 nm, 829.089 nm, and 722.200 nm respectively. This system is a 3-color 3-photon system. If all three lasers irradiate the atomized sample, there is a high probability of ionization of any neutral ground state atoms present in the laser beams. Detuning any one of the lasers reduces the probability of ionization by at least an order of magnitude. Also important for the excitation, and ultimately ionization, of multiple isotopes by the same laser is laser induced bias. LION has been used for

[1] A Pockel's cell is a device to control the modulation of light output.

extensive research to understand the laser induced bias for this and other ionization schemes between different isotopes using measurements of a well characterized standards [22].

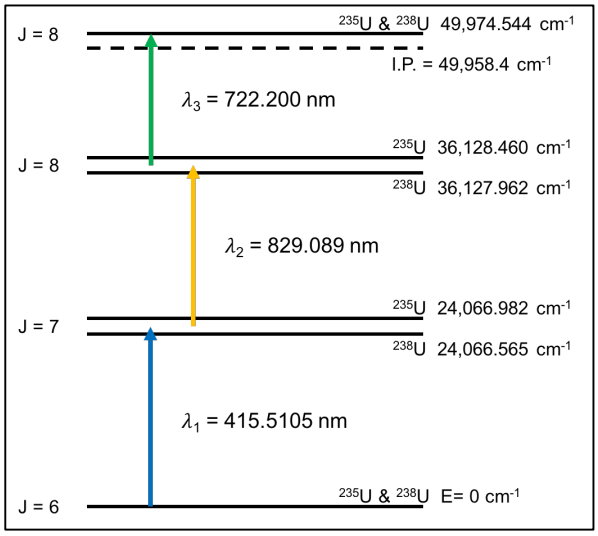

Figure 18. Uranium 3-color excitation scheme. Source: [22].

C. STEP THREE—MASS ANALYSIS AND ION DETECTION

The system that performs the mass analysis and ion detection in LION is a TOF-MS. It consists of a target pedestal, ion lenses, reflectron, and detector. Each is discussed in the detail necessary to understand their function in the greater LION instrument.

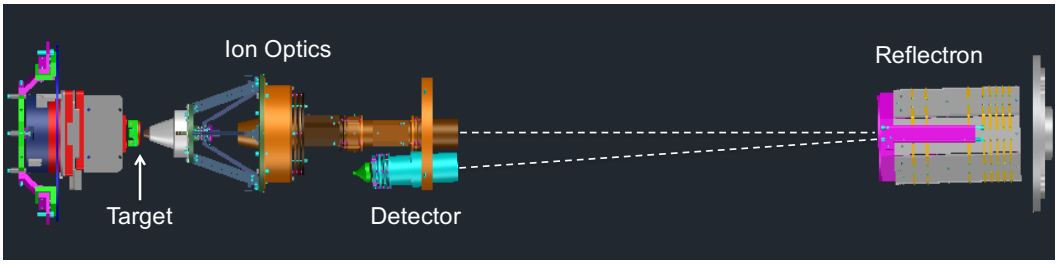

Figure 19. Diagram of the TOF-MS depicting target, ion optics, reflectron, and detector. Source: [8].

The ion optics accelerate ions produced by resonance ionization along the extraction axis. The extraction axis is visualized as a dashed white line on Figure 19. This is done by creating an electric potential. The target stage is positively charged and used to push positive ions toward the ion optics. The ion optics are at ground potential or negatively charged and pull ions through negatively charged ion focusing lenses. These focusing lenses collimate the extracted ion beam.

The reflectron reverses the direction of the ions thereby extending the transit path to the detector while increasing the mass resolution, as illustrated in Figure 20. It uses electric fields to better group the ions of the same mass in space and time prior to arriving at the detector. Particles with a higher kinetic energy arrive at the reflectron before particles with low kinetic energy. The particle with higher kinetic energy will penetrate farther into the reflectron's electric fields. The particle with a lower kinetic energy will arrive later but will reflect out of the reflectron earlier. The result is a better grouping in time, at the detector, of particles with a variation in kinetic energy. As mentioned, secondary ions are extracted with a strong electric field pulse (5 kV). This gives the secondary ions a high enough kinetic energy to penetrate though the reflectron. This means that the secondary ions do not reverse their direction; this is how LION discards secondary ions.

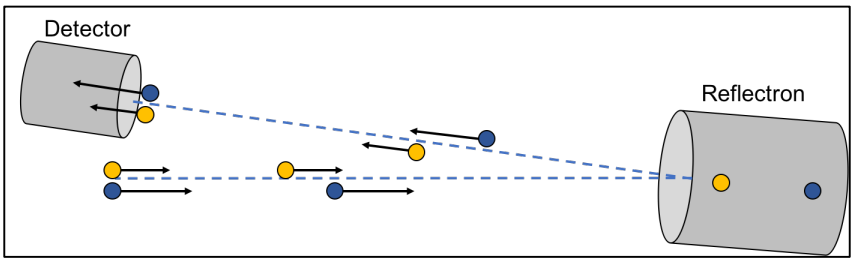

Figure 20. Illustration of reflectron effect in the TOF-MS.

The ions impact a detector at the end of their flight. The ion's impact releases electrons, which are multiplied in the detector to eventually produce an electrical pulse on the detector's anode. Each pulse is considered as one ion count. The arrival time of the ion count by a time-to-digital converter (TDC) relative to the system clock. The TDC

requires approximately 500 ps after each count to dissipate the resulting charge prior to successfully counting another ion. If another ion arrives during that time, it may count both ions as a single count. The accuracy of the ion count is limited by this constraint. To minimize the effect of this limit, the system is kept at a low count rate so that the arrival of two ions within 500 ps is a rare event.

The timing of the electrical pulse from the detector is used to calculate the time of flight of the ion from the time of their acceleration by the extraction voltage between the target and the extraction optics. The beginning of this extraction voltage is considered the beginning of the time-of-flight. An uncertainty is incurred due to the 20 ns length of the ionization laser's pulse. An ion can be produced anytime during this pulse. The end of the time-of-flight is the pulse provided by the detector.

An additional uncertainty is incurred by the random distribution of initial velocities. This random distribution is in both the magnitude and direction of the initial velocity prior to extraction by the ion optics. The distance traveled has an uncertainty due to the volume of the ionization lasers and the kinetic energy distribution of the ablated atoms.

The ionization of the target cloud occurs over a volume in space. That volume can be approximated as a cylinder defined by the cross-section of the laser irradiance and the width of the ablated cloud. Also, particles closer to the point of ablation have a lower kinetic energy than particles farther from the point of ablation. Particles with a kinetic energy with a lower projection onto the extraction axis are harder to focus onto the reflectron and detector. These particles will travel farther because they will oscillate about the extraction axis. This process is illustrated in Figure 22.

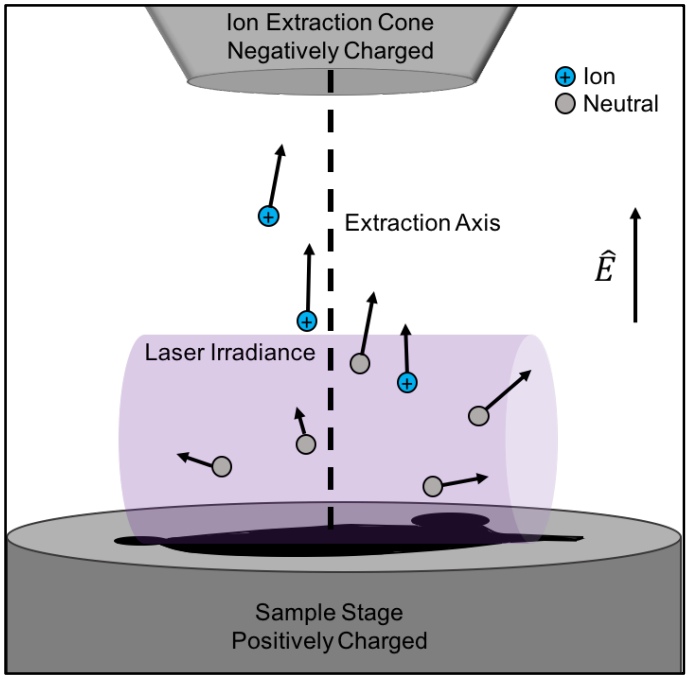

Figure 21. Illustration of the uncertainties incurred by the random velocities and laser ionization beam volume.

The average time-of-flight of the ion depends on its charge-to-mass ratio. Massive particles arrive later than lighter particles. The uncertainty in the time of the ions formation and the distance travelled results in the peaks associated with a given mass-to-charge ratio to have finite widths. The typical width of a peak in this research is on the order of one-half AMU or approximately 0.1 μs. The typical time of flight difference between ^{235}U and ^{238}U is .58 μs.

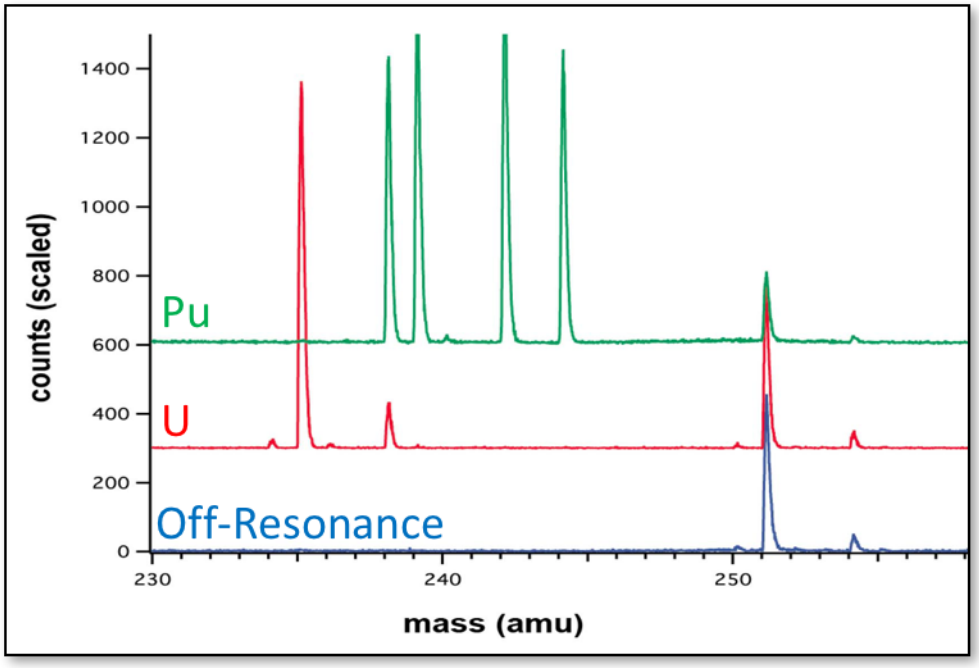

Figure 22. Mass spectra using the LION instrument with lasers tuned to plutonium (Green), uranium (Red), and off-resonance (Blue). Source: [8].

Figure 22 shows the LION capability to selectively ionize uranium and plutonium. The green mass spectrum shows the result of a measurement with the resonance ionization lasers tuned to a plutonium excitation scheme. The red mass spectrum shows the lasers tuned to a uranium excitation scheme on the same sample. The blue shows a mass spectrum with the lasers tuned off-resonance. The peaks have a nearly normal distribution with a width as described earlier. Isotopic ratios are then calculated by summing all the counts arriving within a given peak. Integrating over the width of each peak gives the total number of counts at each mass. In this research, mass peaks were integrated over the range of +/- .5 AMU around the mean mass of a peak. For ^{238}U this equates to a summation of all ions that arrived from 237.5 AMU to 238.5 AMU. In units of time, this equates to a summation over a .2 μs time span. Isotope ratios are inferred by comparing the total number of counts in one peak versus another. This is a simplified version of how LION uses RIMS to produce isotope ratios.

IV. EXPERIMENTATION

This chapter describes three experimental investigations using the LION RIMS instrument. The first investigation, presented in Section A, replaced one of three standard Ti:Saph pulsed laser with a COTS CW laser in the resonance ionization scheme for ^{239}Pu. This experiment was the conclusion of a feasibility study for the use of COTS CW lasers to progress RIMS toward a field deployable system. The second investigation, described in Section B, studied the quantification of saturation curves of a new one- and two-color uranium resonance ionization scheme. The LION team previously identified a one-color two-photon excitation scheme, and then added a second laser (at a different wavelength) to the excitation scheme to access a low-lying state of uranium that is excited during the atomization process. The final investigation, described in Section C, examined carbon coating and implantation methods to improve ablation efficiency and reduce the surface oxidation state on nuclear fallout debris samples. Since this work includes three separate experimental investigations, each section has a description of the setup, procedure, measurements, analysis, and conclusions from each investigation.

A. CW LASER FEASIBILITY STUDY

Part of the ongoing collaboration between the NPS and LLNL focused on conducting feasibility research on paths toward a field-deployable RIMS instrument. This research explored the use of COTS CW lasers as a replacement for one or more of the pulsed lasers in the current LION system. As part of this study, a COTS CW laser was procured by NPS as a substitute for the second excitation laser in the resonance excitation scheme of plutonium.

COTS CW lasers provide third advantages over the current pulsed Ti:Saph cavities used in LION. First, they are much cheaper. The cost reduction is an order of magnitude less. The COTS CW laser used in this experiment was a Sacher Lasertechnik diode laser. It was purchased for approximately $30,000. The LION Ti:Saph lasers are customized cavities that cost on the order of approximately $300,000 each. The second advantage is the complexity and size of the cavities. As shown in Figure 23, the Sacher

laser cavity occupied the volume of a shoe box, approximately 6 x 12 x 5 inch^3. This is much smaller and less complex than the Ti:Saph cavity which occupies approximately a 36 x 24 x 6 inch^3 volume per cavity. The Ti:Saph cavity, as a custom cavity, is a complex and heavily engineered system that consist of numerous mirrors, lenses, diffraction gratings, beam expanders, Pockel's cells, and frequency doubling crystals all mounted on a bread board in open air. Each mount and optic is subject to vibration and thermal effects. A field deployable system must be closer to the manufactured and self-enclosed cavity of the Sacher Lasertechnik laser than the hand assembled and expansive cavity of the Ti:Saph lasers. The final advantage is isotope specificity. The CW laser excites a single isotope at a time because it has a narrow linewidth compared to the broad linewidth of the Ti:Saph lasers. This gives the CW laser the ability to excite only one selected isotope, but also removes the ability to conduct compare isotope ratios in a single measurement.

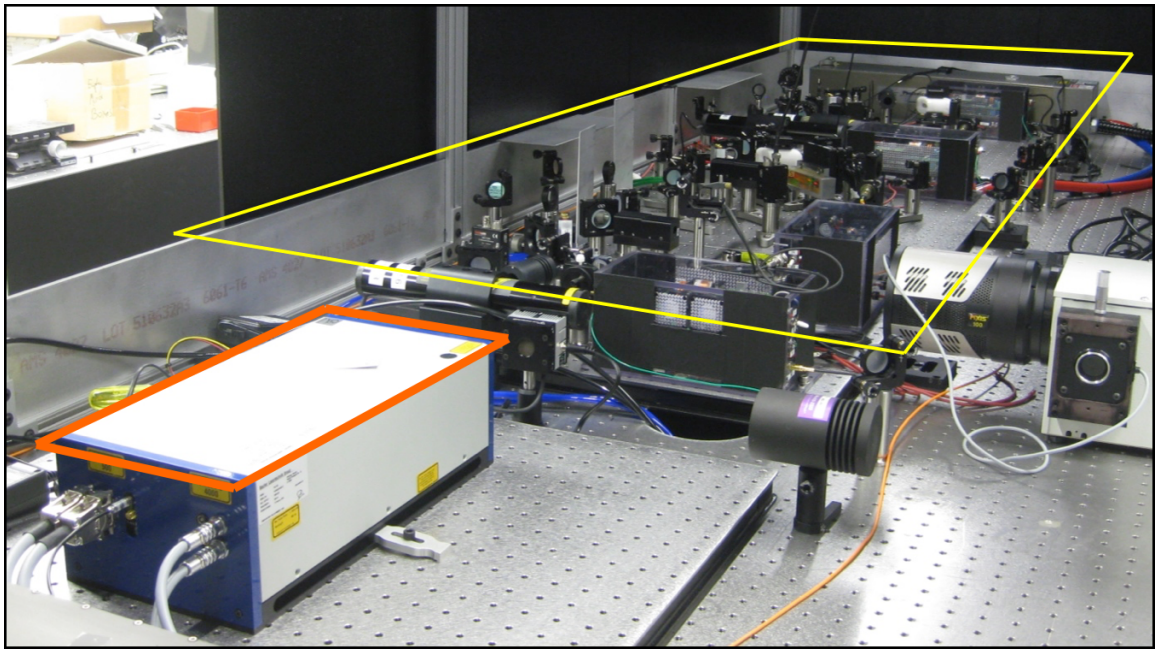

Figure 23. Picture of the Sacher Lasertechnik COTS CW laser cavity (orange) versus custom built Ti:Saph cavities (yellow).

1. Setup

In this first experimental investigation, the Sacher Lasertechnik laser was emplaced in the LION instrument in such a way as to substitute for one of the three Ti:Saph lasers used in the standard 3-color plutonium resonance ionization scheme which is shown in Figure 24. This substitution of the second excitation pulsed laser by the COTS CW laser created a hybrid pulsed-CW RIMS system. The second excitation laser and wavelength is denoted as λ_2. The Sacher Lasertechnik laser has a tunable wavelength range of 840–860 nm. It was manually tuned to 847.274 nm, and the resulting output was verified by a wavelength meter. Manufacturer testing showed the laser attained a power of 2370 mW in the factory. After emplacing the optics required to collimate the CW laser beam with the other two Ti:Saph lasers used in these tests, the measured power just prior to entering the target chamber was 1160 mW or 1.16 W. Measurement of the Sacher Lasertechnik laser's power without additional optics showed a maximum power of 1.8 W. The CW laser bandwidth was reported by the manufacturer to be approximately 100 kHz. Initial testing used a laser beam size of approximately 1.3 mm x 1.5 mm diameter on the major and semi-major axis.

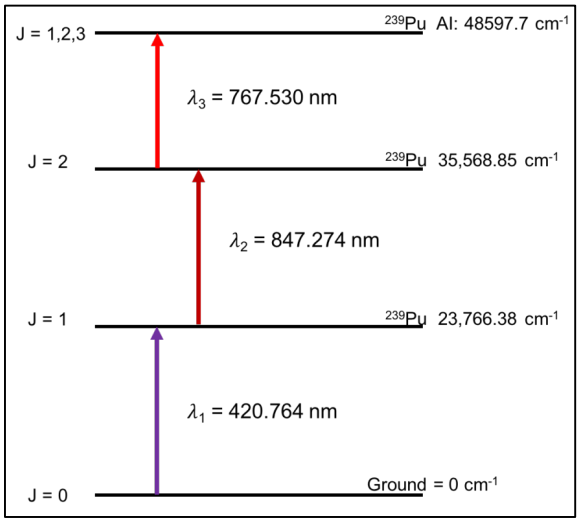

Figure 24. 3-Color Pu resonance ionization scheme showing angular momenta on the left side and the energy in wavenumber on the right side. The second excitation step of this scheme was replaced by a CW laser for this experimental investigation.

2. Procedure

The LION instrument was previously configured to measure plutonium isotope ratios with the pulsed Ti:Saph lasers used for all three steps of the laser excitation scheme. Proper operation of the instrument was confirmed using the excitation scheme shown in Figure 24 on a certified Pu sample identified as CRM137. The measurement resulted in a mass spectrum, as shown in Figure 25, and confirmed that the LION instrument was operating properly.

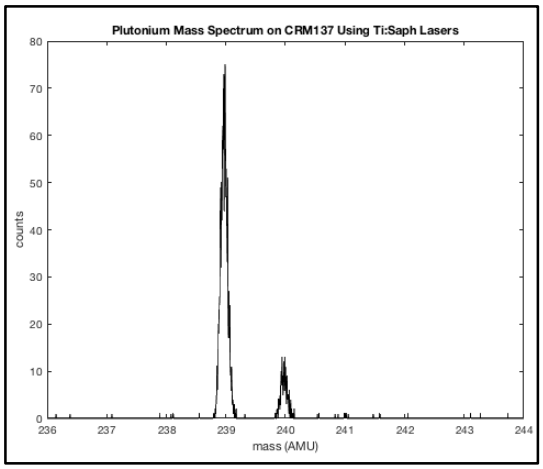

Figure 25. Plutonium mass spectrum of CRM137 prior to CW versus background experimentation to ensure proper LION instrument operation.

After confirming proper operation of the instrument, the goal of the experiment was to validate whether replacing the second excitation laser with the Sacher Lasertechnik CW laser would produce measureable signal from the major Pu isotope, ^{239}Pu. If ^{239}Pu was detected, the CW laser could then be adjusted to the other isotopes of Pu – necessary because of the isotope specificity of the CW laser - so that isotope ratios could then be inferred by interleaving measurements.

Laser ablation in these measurements of the hybrid configuration was accomplished using an 800 nm laser with a 5 ns pulse length. The low parts-per-million in the sample made laser ablation a better option than sputtering as discussed in the method section.

3. Measurement

Six pairs of measurements of the ionization signal of ^{239}Pu versus background signal were interleaved. Ionization signal measurements were conducted with a pulsed/CW/pulsed laser resonance excitation scheme, as described in the Figure 24. Background measurements were conducted with all three laser resonance ionization lasers (pulsed and CW) blocked by shutters to prevent them from entering the target chamber.

Figure 26 shows the results of the measurements described above. The shows the total counts over the six iterations and the uncertainty in the measurement described by the standard deviation. All but one interleaved measurement, the CW result is within one standard deviation of the background ionization result. In two of the interleaved measurements, the CW result is less than the background result. We conclude that these measurements did not show results sufficiently above background ionization for the CW laser to be considered statistically significant. This means that a pulsed/CW/pulsed system did not produce a signal statistically higher than the signal measured without resonance ionization lasers present in the chamber.

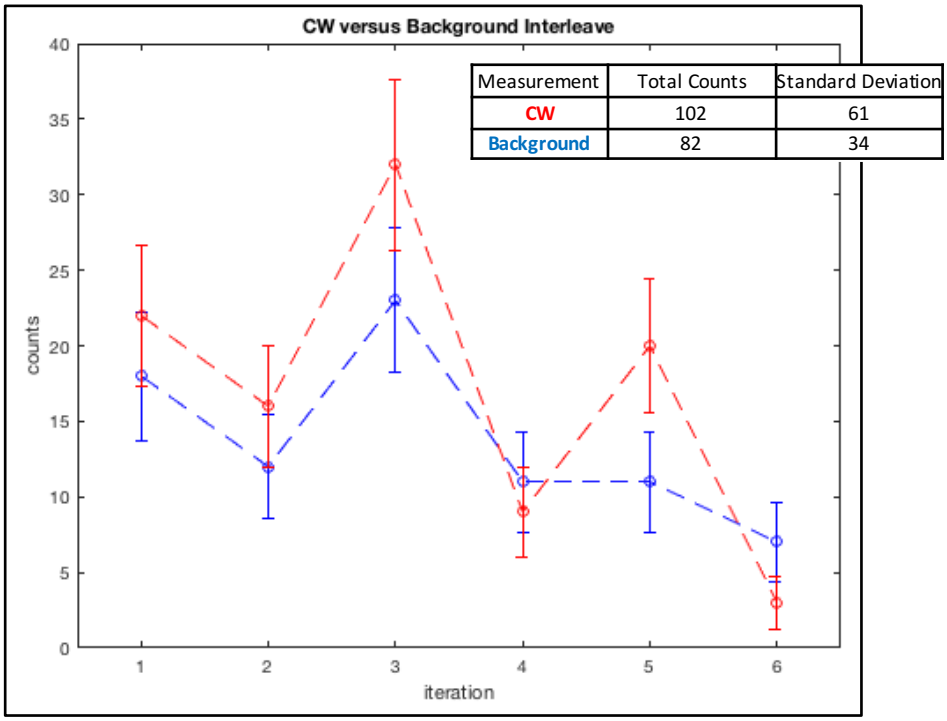

Figure 26. CW to background results of six measurements. Table insert shows the total counts summed over the six experiments with the associated standard deviation.

4. Analysis

Following completion of the above-described tests and arriving at the null result, an analysis was conducted to interpret the implications of the test results. The analysis concluded that the COTS CW laser used in these tests did not produce the power required for stimulated excitation in the current LION RIMS ionization configuration. The LION ionization system is configured to operate at 1 kHz with measurement cycles of 20 ns. That equates to 20 μs of useful irradiance in one second. The operating parameters of LION can be modified such that the time between the first excitation laser pulse and the final ionization laser pulse are separated by approximately 1 μs. That would increase duration of CW laser irradiation by a factor of 500 prior to the final ionization laser's pulse. However, this would not prove to be an effective approach due to the problem of the lifetime of the first excited state.

The recently reported homogeneous lifetime of the first excited state is 9.8 ns [23]. The rate equation for the population of the first excited state, N_1, is

$$\frac{dN_1}{dt} = B_{01}p_1(w)N_0 - B_{10}p_1(w)N_1 - B_{12}p_2(w)N_1 + B_{21}p_2(w)N_2 - A_1N_1 + A_2N_2 \quad (4.1)$$

where N_0 is the population in the ground state, $p_1(w)$, is the frequency dependent power of the first excitation laser, B_{01} is the Einstein B coefficient for the transition from the ground state to the first excited state, and A_1 is the Einstein A coefficient (defined as 1/state lifetime) for decay from the first excited state.

Calculation of the energy delivered per 20 ns pulse shows that the CW laser delivers four orders of magnitude less energy than the corresponding pulsed laser.[2] The broadband pulsed laser delivers approximately 10% of its irradiance within the photon cross section of ^{239}Pu.[3] Adjusting for the 10% means that the pulsed laser delivers a thousand times more energy within the ^{239}Pu cross section than our narrowband CW laser during the 20 ns pulse. Table 1 shows the calculated energy delivered.

Table 1. Comparison of the measured average power for a broadband pulsed .298 W laser operating at 1 kHz with a 20 ns pulse versus a 1.16 W narrowband CW laser to the useful energy delivered to the target isotope.

Laser	Average Power [W]	Energy Delivery (J)
Pulsed	.298	5.96×10^{-5}
CW	1.16	4×10^{-8}

Hutchinson [23] previously conducted experiments and modeling to characterize the saturation of ^{239}Pu ionization as a function of the second-step laser power. Figure 27 shows the measured and calculated power required to saturate the second excitation step of ^{239}Pu from [23]. Comparing Figure 27 and Table 1 shows the pulsed laser drives the

[2] Our CW laser operating at an average power of 1.16 W produces approximately 9.9×10^{10} photons in 10 nanoseconds, or approximately 2×10^{-8} Joules. Our pulsed laser operating at an average power of .298 W with a repetition rate of 1 kHz produces 2.98×10^{-4} Joules per pulse.

[3] The pulsed laser's bandwidth is approximately ten times the Doppler-broadened atomic linewidth. With the laser band center tuned to the ^{239}Pu transition the energy delivered to ^{239}Pu is 2.98×10^{-5} J per pulse.

transition to over 95 percent of the saturation curve. The CW laser delivers three orders of magnitude less energy in the same period. Three orders of magnitude less energy equates to about 0.1 percent of the energy required to saturate the transition.

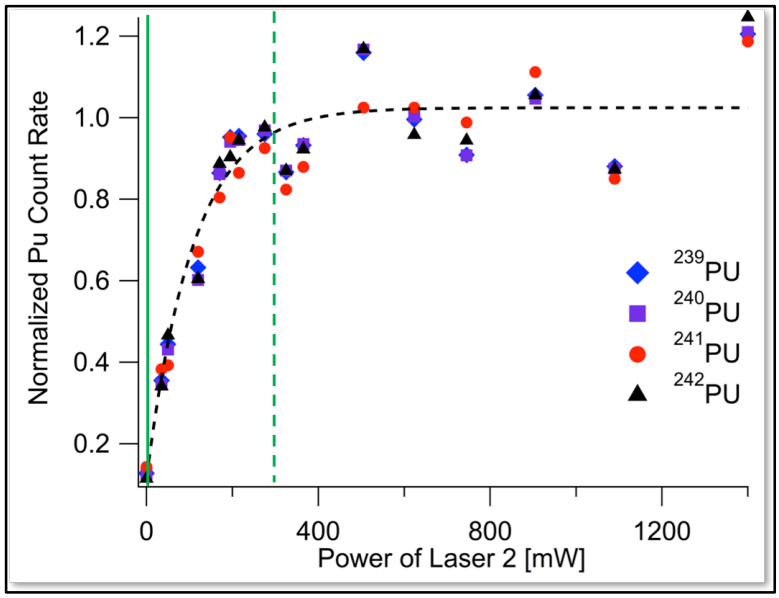

Figure 27. Laser saturation curve for plutonium isotopes. Green lines added by author. Green solid line indicates useful power delivered by Sacher Lasertechnik CW laser at 1.16 W. Green dashed line indicates useful power delivered by a Ti:Saph pulsed laser at an average power of 350 mW. Source: [23].

For the CW laser to achieve the same level of saturation as the pulsed laser, either a longer irradiance time on the target isotopes and/or a much higher average power would be required. While the LION system operates at 1 kHz, delaying the third excitation laser, and target ion collection, by a micro-second is possible but not likely to be effective due to the rapid 9.8 ns lifetime of the second excited state. Equation 4.1 rewritten for the state of the system after the first laser ceases irradiation ($p_1 = 0$), a continuous second excitation ($p_2 \neq 0$), and a delayed third excitation laser ($p_3 = 0$), is shown in Equation 4.2.

$$\frac{dN_1}{dt} = -B_{12}p_2(w)N_1 + B_{21}p_2(w)N_2 - A_1N_1 + A_2N_2 \qquad (4.2)$$

Reviewing the changes leading to Equation 4.2 from Equation 4.1, all terms that included p_1 are zero. In a saturated system, with equal degeneracy, N_0 and N_1 will be equal. This means the target isotopes are equally divided between the ground and first excited states (simplified for equal degeneracies). If p_2 is far below saturation, we can assume N_2 is much less than N_1. Re-writing Equation 4.2 with these assumptions results in Equation 4.3.

$$\frac{dN_1}{dt} = -B_{12}p_2(w)N_1 - A_1N_1 \tag{4.3}$$

Equation 4.3 has two terms. The first term is the rate at which stimulated excitation transitions an atom from the first excited state to the second excited state. The second term accounts for spontaneous decay from the first excited state down to the ground state. In our experiment and follow-up calculations, we determined that the CW laser power, p_2, is insufficient to overcome the spontaneous decay. This means more atoms will decay to the ground state than the number of atoms that will be excited to the second excited state. By the time the third excitation laser begins irradiating, the population in the second excited state, N_2, is negligible compared to background ionization.

5. Conclusion

The experiments presented here describe a final effort to document the conclusion of the CW laser feasibility study. Numerous other experiments were conducted with similar null results. The analysis described in this thesis suggests that a hybrid Pulsed/Continuous Wave/Pulsed system would be impractical, based on the current pulsed laser excitation scheme. An alternative and more practical path to ionization with commercially available lasers could be a CW/CW (or CW/CW/pulsed) system. Such systems have shown utility in detecting trace U isotopes [24]. The effective use of CW lasers in such systems requires a geometry for ionization that significantly increases the time atoms interact with the laser beams. This could be accomplished by replacing the laser ablation system with a tube furnace, such that atoms must interact with the CW laser beams over a significant length as they diffuse out of the tube. The useful yield of this system is considerably less than a pulsed system, but is capable of selectively ionizing

single isotopes and has utility in measuring trace isotopes where the major isotope is 10^5–10^6 time more abundant [24].

Such an approach could be applied to Pu measurements. With adjustable frequencies that span the Pu isotope shifts, a series of CW lasers could target each isotope of plutonium at all three excitation steps [25]. A forward deployed system, in this configuration, could confirm the presence of any plutonium isotope in a matter of hours from intercepted illicit material or post-detonation debris.

Continued research aims at finding long-lived excited states capable of facilitating a longer irradiance time by a CW laser. A two-photon, single-color system with a long-lived first excited state would be ideal for the creation of a single CW laser RIMS system. Recent research at LLNL has identified alternative excitation schemes [8]. The next section covers a one- and two-color uranium excitation scheme that uses only one excitation state followed by ionization. This reduces the number of transitions required from 3 to 2 and the number of lasers required from 3 to 1. Further research on this idea could offer a trace-detection uranium instrument with only one CW laser.

The LION system continues to enable research and progress towards rapid isotopic analysis in a post-detonation scenario using RIMS. While the primary goal is isotopic ratio measurements with a high degree of certainty, an ancillary future goal is a field deployable system. CW laser technology is not promising in a hybrid pulsed/CW scheme operating in a configuration like that of LION. Alternative system configurations, such as firing the excitation lasers paraxial to the ion optics, could provide a means of trace actinide detection in post-detonation environments. Currently, pulsed lasers provide the only practical means for full laser saturation of multiple isotopes in a single pass.

B. SIMPLIFIED IONIZATION SCHEMES FOR URANIUM

As the resonance ionization process is the most important step in RIMS, an essential field of study for the optimization of RIMS is a simplified laser resonance ionization scheme for uranium. Prior spectroscopy studies provide numerous highly selective schemes for uranium. Figure 18 in the method chapter shows one such 3-color 3-photon scheme. As RIMS progresses toward a field-deployable system, complexity and

cost of the instrument become important factors to consider. The reduction in the number of lasers required for resonance ionization accomplishes both a reduction in the complexity and cost of a future field deployable instrument. Past spectroscopy research did not focus on simplified excitation schemes, such as the one described in this section. The one- and two-color schemes presented in this section were a recent discovery by the LION team.

1. Setup

A one-color ionization scheme was identified by the LION team at LLNL. This one-color, two-photon excitation scheme uses a single laser beam with a wavelength of about 396 nm to resonantly ionize uranium. Following initial tests of the single laser resonance ionization scheme, the idea of using a second laser to access a low-lying excited state known to be populated during sputtering was also tested. This low-lying state population was quantified as 20% +/-6% of the total atomized uranium in [26]. The low-lying state of 620 cm^{-1} requires a roughly 406 nm laser to transition to the same first excited state, 25,253 cm^{-1}, as in the 396 nm one-color scheme. The resonance excitation schemes are shown in Figure 28.

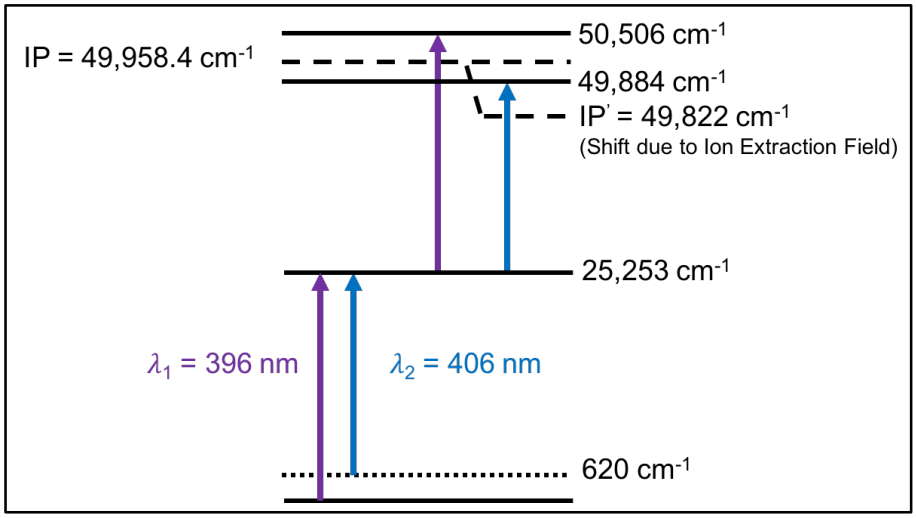

Figure 28. One and two-color uranium laser resonance ionization schemes shown with the utilized excited state and ionization levels with associated energy in wavelength. The 396 nm scheme populates a possible AI state above the IP. The 406 nm scheme populates a possible Rydberg state below the IP. The Rydberg state is ionized by the shift in the IP caused by the ion extraction field.

2. Procedure

A certified standard was used for these measurements. The standard, CRM125A, is a certified uranium fuel pellet of UO_2 enriched to approximately 4% ^{235}U. For this experiment one of the Ti:Saph cavities was tuned to 792.527 nm and then doubled to the second harmonic with a lithium triborate crystal to 396.264 nm. The beam size of this laser was 1.1 mm x 1.2 mm in diameter on the major and semi-major axis. A second Ti:Saph was tuned to 812.499 nm and then doubled to the second harmonic of 406.250 nm by the same method. The beam size of this laser was 1 mm x 1.2 mm in diameter on the major and semi-major axis. Both lasers were reflected once back through the target chamber to account for Doppler broadening. Atomization was accomplished by ion sputtering with an the Ionoptika ion gun using gallium ions (Ga^+) at 15 keV for a 300 ns pulse. The surface was cleaned in raster mode with a 10 x 10 micron^2 area with the same Ga^+ ions for two minutes prior to each experiment. Surface cleaning prior to measurement reduces uranium oxide molecule formation during the atomization step. Each experiment consisted of 10,000 measurements at a repetition rate of 1 kHz. In each

experiment the surface was cleaned for 2 minutes with Ga^+ ions and measured for 10 seconds (10,000 shots at a rate of 1 kHz).

3. Measurement

The first measurement was to determine the power required to saturate the ionization of the uranium atoms. The atomized cloud is considered saturated by the laser when increasing the laser power does not significantly increase the ion signal. Table 2 shows the saturation curve data for the 396 nm laser alone. For this test, the 406 nm laser was blocked and not allowed into the target chamber. The laser power was measured prior to each measurement and was varied from 2 mW to 525 mW. Figure 29 shows the saturation curve of normalized counts versus laser power with a line fit to emphasize the curve. The curve shows that 650 mW drove the curve almost to saturation, but the curve cannot be considered saturated at this beam size.

Table 2. Laser power versus ion counts for 396 nm one-color two-photon uranium excitation scheme. The final column is normalized to 1 for the highest count achieved.

Laser Power (mW)	Counts	Normalized Counts
650	55216	1
525	49211	.891245291
450	46128	0.835410026
350	40207	0.728176615
250	35000	0.633874239
140	24687	0.447098667
48	12014	0.21758186
2	349	0.011753839

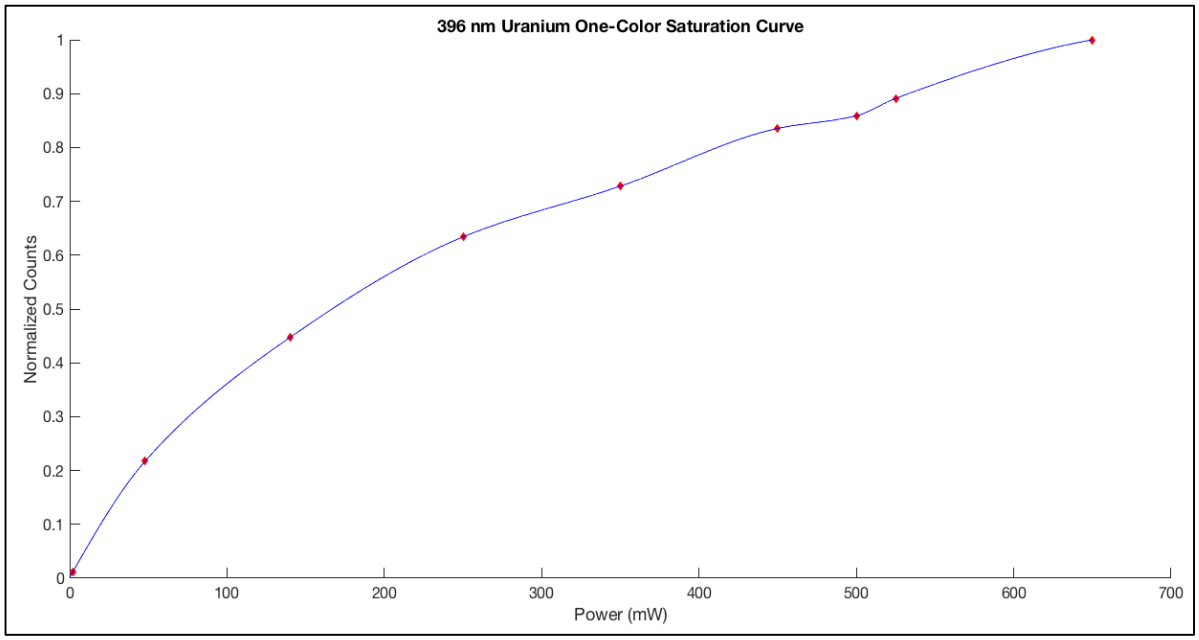

Figure 29. Saturation curve of one-color uranium scheme. Red Points: Experimental Data. Blue Line: Line Fit.

Similar procedures for testing the one-color saturation curve were followed in the testing of the two-color scheme. The one-color laser, 396 nm, was kept at a power of 650 mW. The low-lying excited state laser, 406 nm, was varied to produce a saturation curve. The ion counts versus laser power of the low-lying state laser are shown in Table 3. Normalized counts versus laser power is plotted with a line fit to emphasize the curve in Figure 30. The counts were normalized to 1 for the highest count achieved.

Table 3. Laser power versus ion counts for the low-lying state uranium excitation scheme. The final column is normalized to 1 for the highest count achieved.

Laser Power (mW)	Counts	Normalized Counts
660	88733	1
640	88312	0.98744
540	86604	0.93648
420	83841	0.85404
330	81593	0.78697
215	78989	0.70928
36	73202	0.53662
0	55216	0

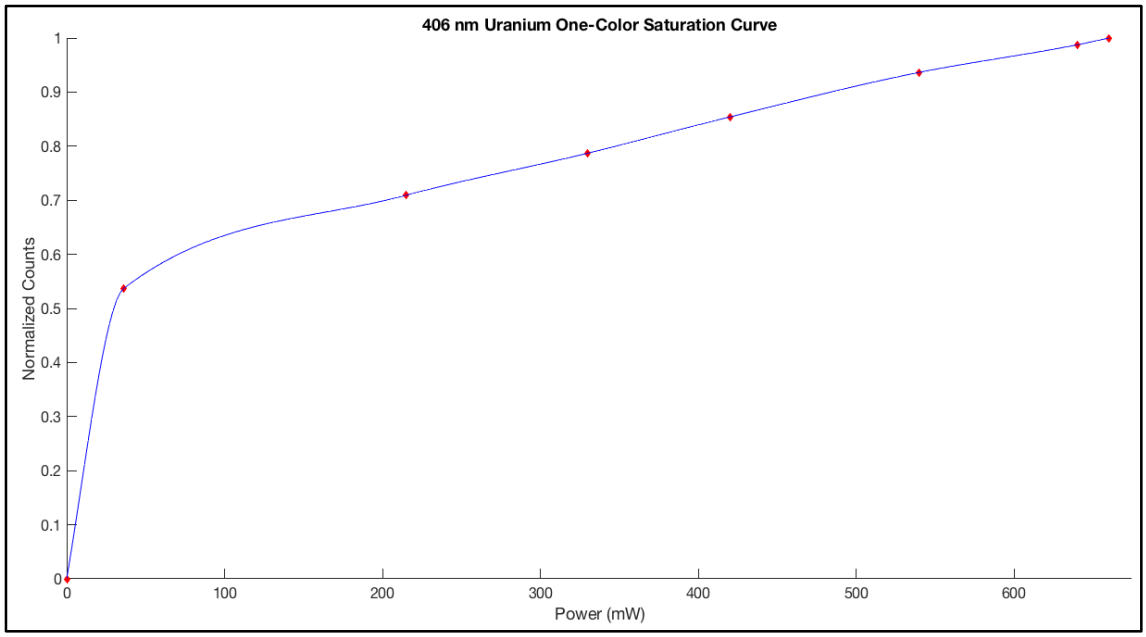

Figure 30. Saturation curve of two-color uranium scheme varying the low-lying state laser (496 nm). A 396 nm laser was held constant at 650 mW. Red Points: Experimental Data. Blue Line: Line Fit.

A final test measured the signal produced from the 396 nm laser alone, then the 406 nm alone, and finally, the signal measured from both simultaneously. The results are shown in Table 4.

Table 4. Uranium ion signal from 396 nm, 406 nm, and then both on CRM125A uranium sample.

Laser	Ion Counts
396 nm	55216
406 nm	11823
Both	88733

4. Analysis

Uranium was successfully resonantly ionized with high probability using a single 396 nm Ti:Saph laser. A second Ti:Saph laser, tuned to 406 nm, accessed a low-lying excited state and increased the signal by 62% over the one-color scheme alone. An increased efficiency was seen from the two-color scheme over either 396 nm or 406 nm alone, even if summed together. This indicates that the ionization states reached using the 396 nm and 406 nm wavelength lasers have different ionization probabilities.

Transitioning from the first excited state (25253 cm^{-1}) with a 396 nm photon results in an energy (50506 cm^{-1}) above the IP (49958.4 cm^{-1}). This transition could be either an AI state or ionization into the continuum, the strong ionization probability favors this being an AI state. Transitioning from the first excited state with a 406 nm photon results in an energy (49884 cm^{-1}) below the IP (by 74 cm^{-1}). This is likely a Rydberg state.

If a Rydberg state exists at 49884 cm^{-1} and it can be ionized by the ion extraction pulse on LION. The change in electric potential due to an external electric field is expressed in Equation 4.4,

$$\Delta E = 6.1\sqrt{\varepsilon} \tag{4.4}$$

where ΔE is the change in energy due to an external electric field and $\mathcal{E}$ is the amplitude of the electric field in volts per centimeter [27]. The resulting shift in potential is in units of cm^{-1}. For the LION system, the electric field gradient is approximately 500 V/cm^{-1}. This results in a downward shift of the ionization potential of uranium by approximately 136 cm^{-1}. This calculation explains why the 406 nm laser can ionize uranium in the

absence of the 396 nm laser. The sharp rise at very low power is explained by the presence of the 396 nm laser causing a higher rate of transition to a state above the IP with a high probability of transition. This dynamic is best displayed in Figure 31.

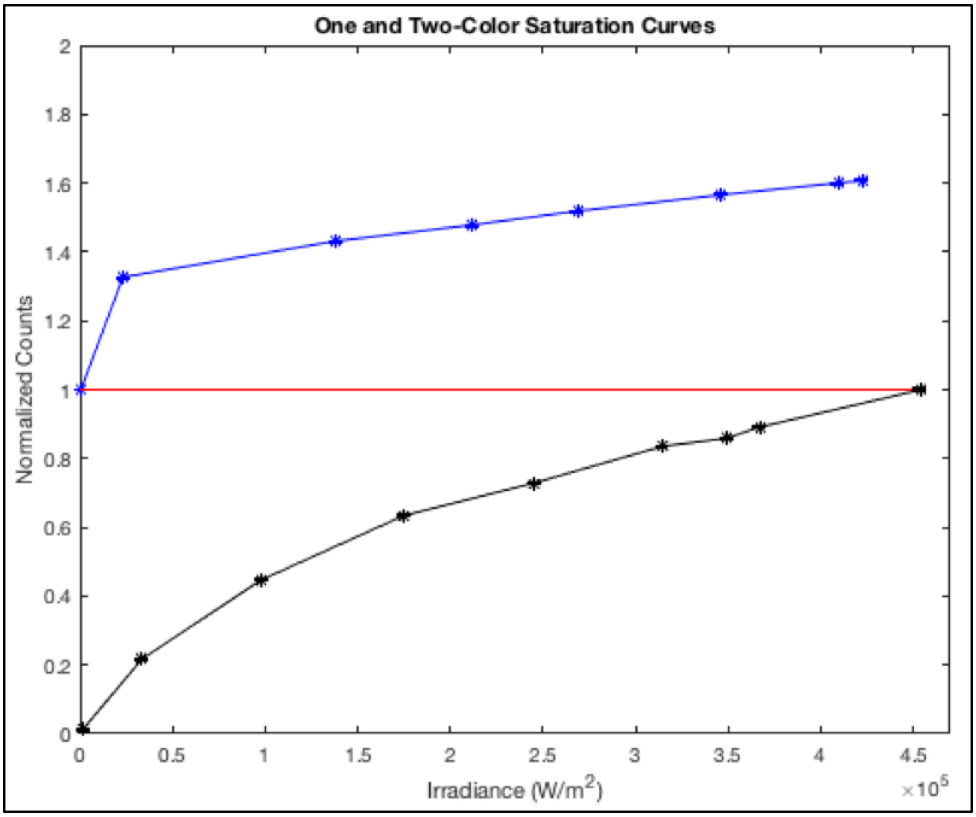

Figure 31. One- and two-color saturation curves for uranium using a known sample; CRM125A. Black: 396 nm alone. Blue: 406 nm varied with 396 nm held constant and normalized to 1 from the 396 nm laser. Red: normalization count line for 406 nm saturation curve.

5. Conclusion

This experimental investigation shows that both a one-color uranium scheme and two-color uranium scheme can be driven to near saturation with power below 1 Watt at 1 kHz. The one-color scheme offers a potential alternative to multiple laser systems. A one-color system reduces the engineering complexity of a future field-deployable system and provides a simplified setup even in a laboratory setting. A system using the one-color

uranium scheme can provide early timeline solutions, free of isobaric interferences, capable of deploying closer to any possible incident requiring isotopic analysis.

The two-color uranium scheme shows an increase of approximately 62% in the ion counts versus the one-color uranium scheme. This scheme offers a new standard excitation scheme capable of replacing the current three-color scheme. This also offers reduced complexity in the LION instrument with increased efficiency. These schemes offer easily achievable optimization paths.

C. SURFACE REDUCTION USING CARBON COATING AND IMPLANTATION

This section chronicles the experimental investigation to increase the efficiency of laser ablation and reduce the oxidization state of the surface of nuclear fallout debris with carbon coating and then carbon implantation. Carbon implantation was conducted for the first time on the LION instrument during this experimental investigation. Methane was used as a carrier for the carbon. The methane was ionized and used to sputter the surface resulting in the implantation of carbon and hydrogen near the sample surface.

This section begins by presenting initial attempts to analyze uranium directly from fallout with a carbon coating. Samples imaged by a scanning electron microscope (SEM) are often coated with thin (~2-10 nm) layers of carbon prior to imaging to prevent charging of the sample during imaging. Samples tested by LION are often received by the LION team after SEM imaging with a carbon coating. Previous testing of these samples showed strong ion signals in the uranium atom region. Figure 32 shows elemental mapping conducted by SEM on a fallout sample. This sample is referred to as Sample 1. It is described here based on its past testing. In the present research, discussed in the measurement section, it was also recoated with carbon and tested again for this experimental investigation.

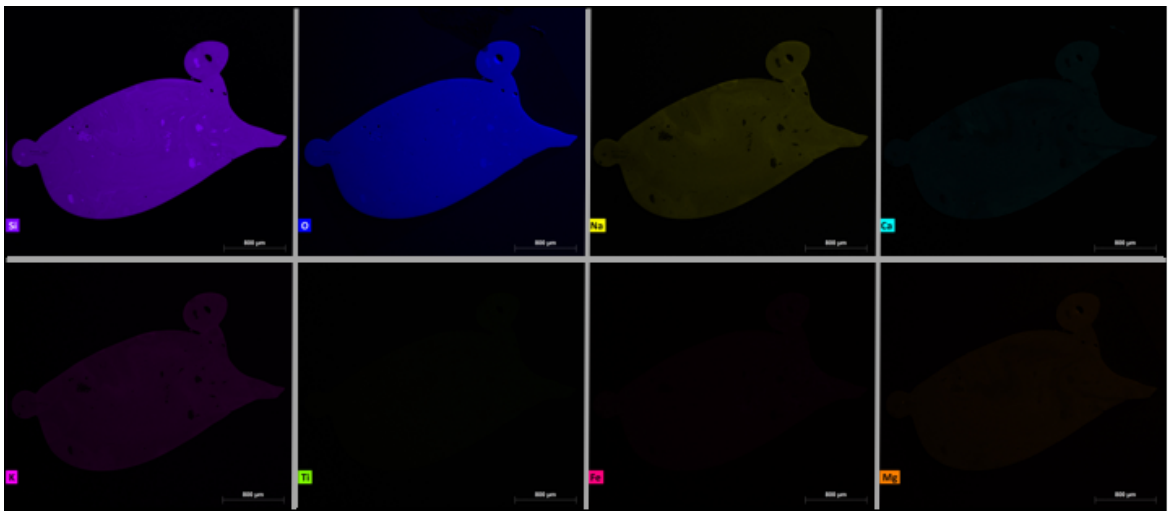

Figure 32. SEM mapping of multiple elements in Sample 1. First Row Si, O, Na, Ca. Second Row K, Ti, Fe, Mg.

In experiments conducted prior to this investigation, testing of Sample 1 with a carbon coating produced clear uranium ion signals in the uranium region of interest when ablated by an 800 nm pulse lasting 5 ns and subjected to the nominal LION RIMS configuration. Figure 33 shows the mass spectrum in the uranium atomic and molecular mass region of 230–270 AMU. Figure 34 also shows a closer view of the uranium atomic region from 230–240 AMU. The fallout sample showed a high-concentration of ^{235}U and ^{238}U. The $^{235}U/^{238}U$ ratio was quantified as $1.78 \pm .03$ in the spot measured. Two smaller mass peaks are visible at 232 and 234 AMU. This is ^{234}U and possibly ^{232}Th or a molecular interference. The $^{234}U/^{238}U$ ratio was quantified at $0.018 \pm .003$. These ratios were consistent with prior testing of fallout that quantified the mixing of the uranium from the nuclear device with natural uranium from the environment surrounding the device as shown in Figure 35. Uranium isotopes are known to vary over several orders of magnitude within a given sample of fallout [12]. There is also a peak at mass 256 AMU that cannot be identified as to its molecular composition. These results were the motivation for this experimental investigation.

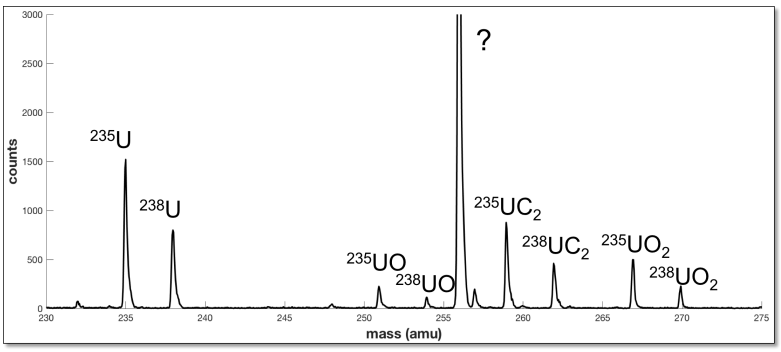

Figure 33. Mass spectrum of the atomic and molecular uranium region from initial carbon coating test of Sample 1.

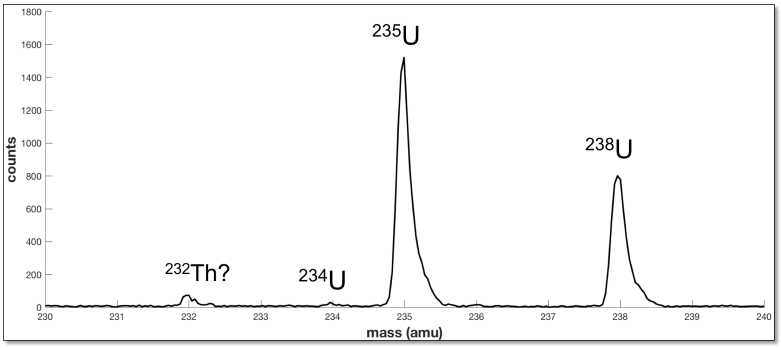

Figure 34. Mass spectrum of the atomic uranium region from initial carbon coating testing of Sample 1.

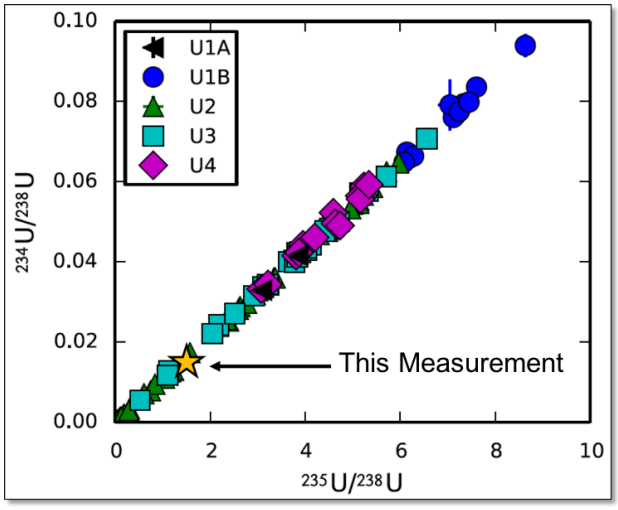

Figure 35. A graph of $^{234}U/^{235}U$ ratio versus $^{235}U/^{238}U$ ratio. Gold star and arrow added to represent the data collected by LION. The uncertainty is on the order of the symbol size. Source [12].

The carbon coating of the sample showed an increase in the ability of the ablation laser to transfer heat into Sample 1 and provided an isotopic ratio that fit prior historical fallout research [12]. Over time, the amount of material ablated per laser pulse from the sample decreased. This is theorized to be the result of the carbon coating being ablated from the surface. The postulated explanation is that once the surface is cleaned of carbon, the laser stops coupling well to the sample and the signal drops significantly. Figure 36 shows Sample 1 after initial testing. Dark spots represent laser ablation scars. Measurements of the sample after laser ablation showed these dark spots were not definitive topographical features. They measured only nanometers deep over distances of microns.

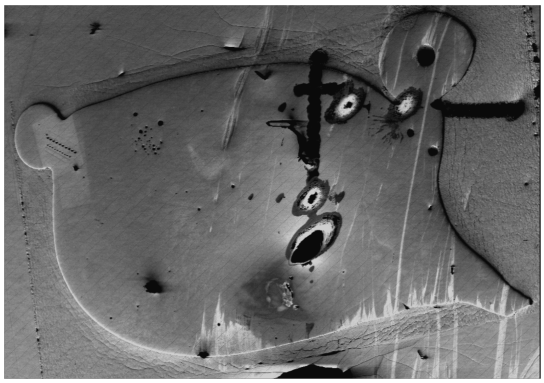

Figure 36. SEM image of Sample 1 after initial testing. Laser ablation scars appear as dark marks where carbon was removed.

After promising initial results, the motivation for the further testing of carbon coating on fallout samples was that carbon is opaque to the ablation lasers currently available to LION. An opaque material absorbs laser energy as heat. Surface coating with such an opaque material enables improved transfer of heat to the surface of the coated sample. It must also be noted that laser ablation is the preferred ablation method because ion sputtering does not remove the amount of material necessary to measure the small concentrations of SNM diluted into the soil and consistently overcome background; SNM in nuclear fallout is regularly on the order of a parts-per-million in concentration.

Therefore, laser ablation is the best option for atomization. Also, laser ablation is less sensitive to non-conducting samples than ion sputtering, such as silicate fallout.

This experimental investigation also measured the effects of carbon implantation into the surface of nuclear fallout debris. A postulated advantage of carbon implantation was to increase the laser ablation efficiency by providing an opaque material near the surface of the silicate fallout sample and cause a reduction of uranium oxidation in the surface. Implanted carbon was expected to bind with oxygen near the surface. Reducing the oxygen available to form uranium oxide molecules was expected to increase the uranium available as an atomic species. This reduction mechanism was expected to increase atomic ^{235}U and ^{238}U signal versus the background noise signal.

1. Setup

The experiments of this investigation re-examined carbon coating and then measured the effect of carbon implantation on RIMS analysis of Sample 1. A second sample referred to as Sample 2, shown in Figure 37, was also tested for the effects of carbon coating. Samples 1 and 2 were received with a carbon layer about 5 nm thick coated across the surface. For the tests with Sample 1, it was re-coated for this experimental investigation.

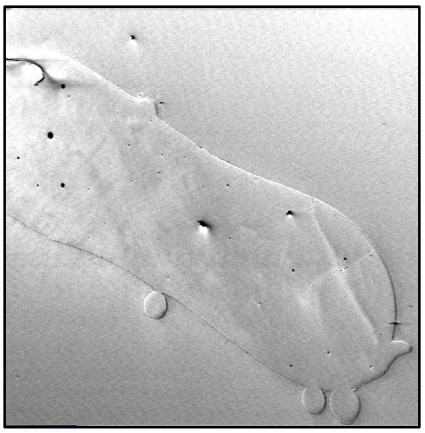

Figure 37. SEM image of Sample 2 prior to testing.

After testing the samples with the carbon coating, a portion of the surface of Sample 1 was cleaned with argon ions (Ar^+) to remove the remaining surface coating of carbon. The clean portion of the surface of Sample 1 was then implanted with methane ions (CH_4^+). The methane was implanted in the same manner as ion sputtering as discussed previously in the theory and method chapters.

2. Procedure

To explore the impact of carbon coating and implantation, three separate measurements were made in this experiment. First, mass spectra were produced by RIMS from Sample 1 with a carbon coating. Next, a mass spectrum from Sample 2 was tested in the same manner as Sample 1. Finally, Sample 1 was cleaned of surface carbon and implanted with carbon in the form of methane ions (CH_4^+) to measure the effect of carbon implantation on the sample surface.

A Nd:YAG, 1064 nm, was used for laser ablation during each of these experiment. The Nd:YAG operated at 20 Hz as opposed to the 1 kHz frequency normally used for RIMS measurement with the LION system. The system's timing was altered to trigger measurements at 20 Hz to accommodate the lower pulse frequency Nd:YAG flash lamp. Resonance ionization was accomplished by the two-color uranium scheme discussed in section B of this chapter. The system otherwise operated under normal operating procedures for the testing of the carbon coatings and carbon implantation.

Prior to carbon implantation, the surface was cleaned of the carbon coating. The cleaning was accomplished by ion sputtering with Ar^+ for 4 minutes at 160 nA with a spot size of 1.7 x .8 mm^2. Sputtering the surface with Ar^+ removed any remaining carbon coating.

Finally, methane was introduced into the LION system through the Hiden gas gun. Methane gas is the most abundant gas that contains carbon, but does not contain oxygen. Using any gas containing oxygen would be counterproductive to oxidation reduction efforts. Methane was used to implant the surface and introduce a dose of carbon to measure the effects. Implantation consisted of two separate doses consisting of 4 minutes of methane at a current of 270 nA, as measured at the target platform with a

Faraday cup, on a spot size of 0.17 x 0.08 cm^2. A simple derivation can calculate the dose ions per cm^2. Current is in units of coulombs per second. Multiplying this by time results in the units of coulombs. Dividing this value by the charge of an ion, the elemental charge, you get the number of ions delivered by a known ion current during a known time. Dividing by the area in cm^2 results in a calculation of the dose in ions per cm^2. This logic is expressed in Equation 4.5. Using Equation 4.5, this results in a dose of 2.97 x 10^{16} ions/cm^2. After two doses, this equates to 5.95 x 10^{16} ions/cm^2. These values are the number of methane ions implanted and equal to the number of carbon ions implanted in the sub-surface region.

$$Dose = \frac{Current \times Time}{Area \times Elemental\ Charge} \tag{4.5}$$

3. Measurement

Both samples were tested for the effect of carbon coating on laser ablation. While the coating did provide an increase in ablation of the normally transparent materials, Sample 1 and Sample 2 gave distinctly different signals. A broad spectrum and uranium region of interest mass spectrum are shown in Figure 38.

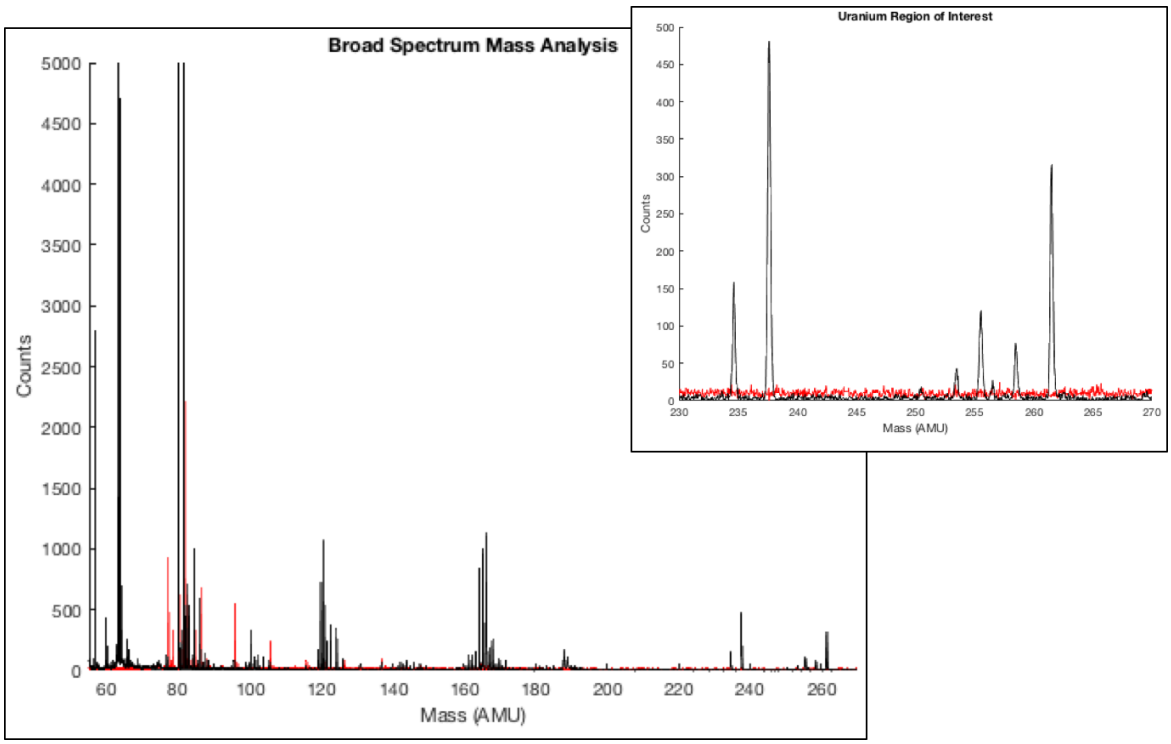

Figure 38. Mass spectrum of Sample 1 and 2 with carbon coating. Large graph spans 55–270 AMU. Smaller graph shows the uranium region of interest 230–270 AMU. Black: Sample 1 and Red: Sample 2.

The two experiments showed different ablation behaviors in the uranium mass region. Sample 1 produced definitive ^{235}U and ^{238}U atomic peaks with oxide (251 and 254 AMU) and dicarbide (259 and 262 AMU) peaks. The peak at 256 AMU is unknown, this peak is also apparent on the prior spectrum of Sample 1 in Figure 33 from prior testing. Compared to Sample 1, Sample 2 did not produce definitive peaks in the uranium atom or molecular region. In fact, it showed less signal throughout the measured mass region. Both samples show similar ablation when inspected by SEM. Figure 39 shows Sample 1 after laser ablation with the Nd:YAG laser. Figure 40 shows Sample 2 after laser ablation. Figure 41 shows an SEM pictures showing the effects of Ar^+ cleaning to remove the carbon coating from Sample 1 prior to carbon implantation.

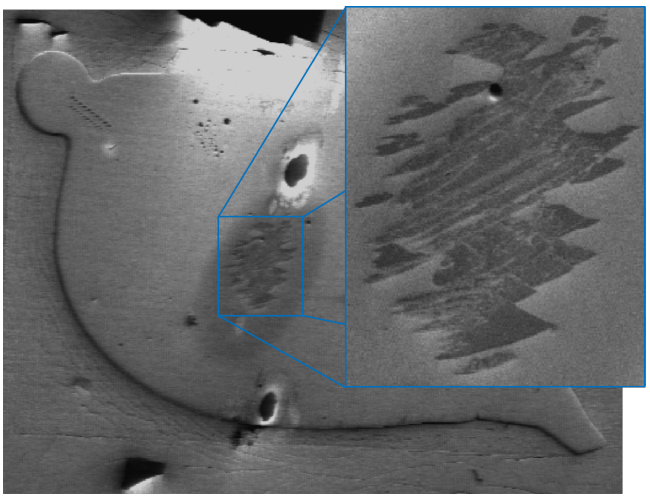

Figure 39. A SEM image of Sample 1 showing laser ablation scarring caused during laser ablation of a carbon coating.

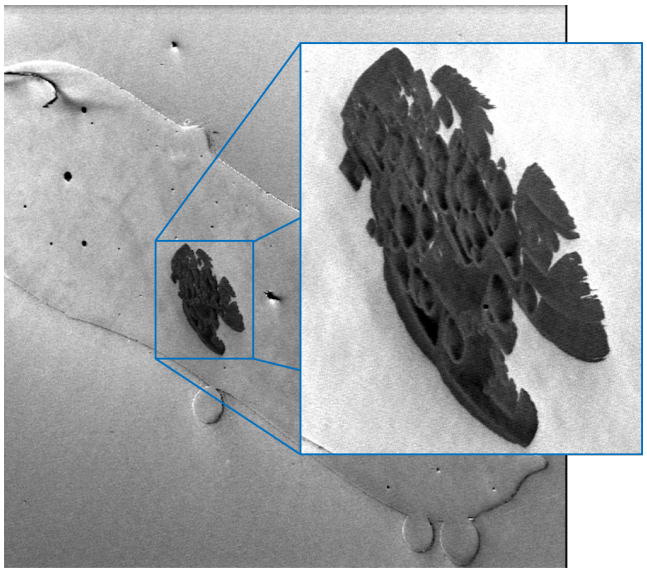

Figure 40. A SEM image of Sample 2 showing laser ablation scarring caused during laser ablation of a carbon coating.

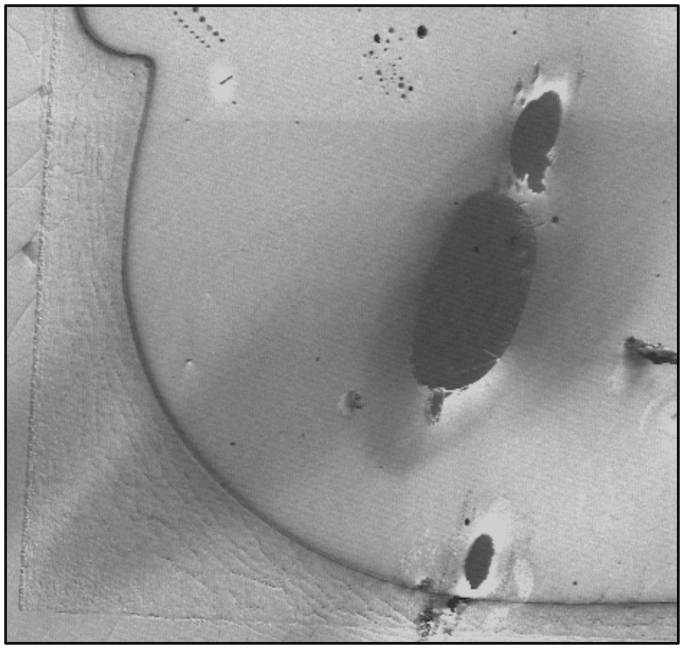

Figure 41. SEM image of nuclear fallout Sample 1 after Ar^+ cleaning. Dose of 1.76×10^{16} Ions/cm^2.

For the carbon implantation testing, three mass spectra were collected from Sample 1. The first mass spectrum was collected on Sample 1 after the Ar^+ sputtering. It showed definitive mass peaks in the atomic, oxide, and carbide mass regions. Prior to taking additional spectra, the surface was implanted with a dose of carbon. Carbon implantation was accomplished by impacting the surface with high energy, 3 keV, methane ions (CH_4^+). CH_4^+ implantation was conducted for 4 minutes followed by a measurement. After the first carbon dose, a mass spectrum was collected. This process was repeated with an additional 4-minute dose followed by a third and final mass spectrum being collected. An image of Sample 1 is shown in Figure 42 after carbon implantation. Figure 43 shows the result of the mass spectrum measurements and the correlating uranium signal to noise ratios. The counts for each uranium isotope were summed from counts +/- .5 AMU around the center of the isotope mass. The noise value was calculated from the counts for a mass of 237 AMU. The results for the experiment show an increase of the in the uranium signal-to-noise ratio from 5.4 to 13.9.

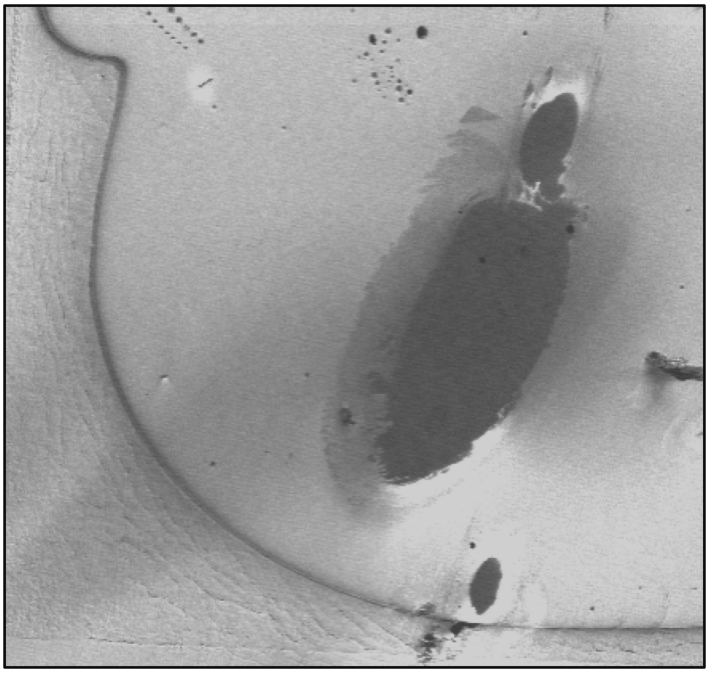

Figure 42. SEM image of Sample 1 after carbon implantation. Total dose of 5.95 x 10^{16} Ions/cm^2.

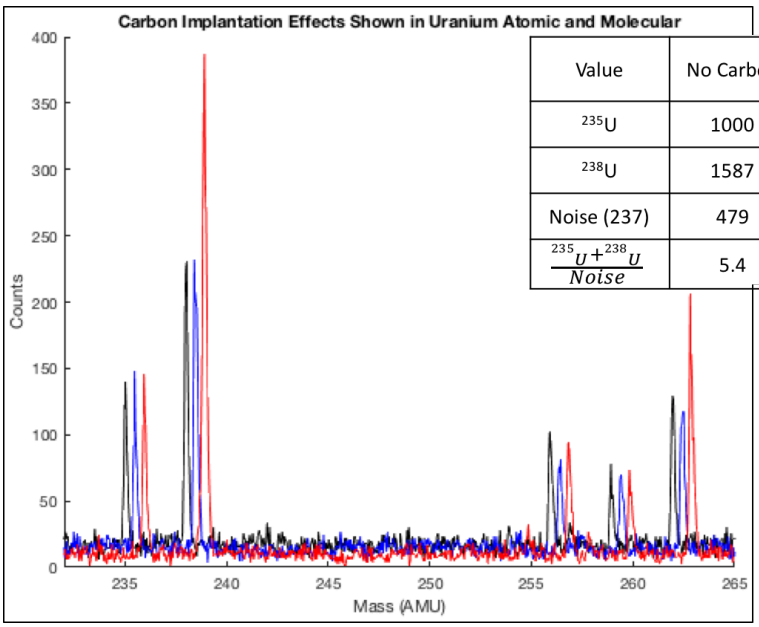

Value	No Carbon	4 min Methane	8 min Methane
^{235}U	1000	964	961
^{238}U	1587	1685	2633
Noise (237)	479	340	259
$\frac{^{235}U+^{238}U}{Noise}$	5.4	7.8	13.9

Figure 43. Mass spectrum of Sample 1 during a carbon implantation experiment with table of ^{235}U counts, ^{238}U counts, noise counts, signal-to-noise ratio included. Black: After Ar^{+} sputtering. Blue: 4 minutes methane ion sputtering (Shifted right .5 AMU). Red: 8 minutes total methane ion sputtering (Shifted right 1 AMU).

4. Analysis

Sample 1 and Sample 2 showed dramatically different mass spectra during laser ablation measurements with a carbon coating. Sample 1's mass spectrum showed definitive mass peaks in the uranium region of interest spanning 230–270 AMU. Sample 2 did not show definitive mass peaks in the uranium region of interest. Because Sample 2 is a historic fallout debris sample, it is unclear without further testing if this mass spectrum is consistent with the composition of the sample as a whole or an effect of the carbon coating. The carbon coating did increase the efficiency of laser ablation on both samples.

Carbon implantation on Sample 1 increased the uranium signal-to-noise ratio. The results for the experiment show an increase of the uranium signal-to-noise ratio from 5.4 to 13.9. During carbon implantation, the ^{238}U signal increased significantly without a proportional increase in ^{235}U. It could be due to a significant difference in the uranium content in the surface between measurements. The uranium atomic (235 and 238 AMU)

and dicarbide (259 and 262 AMU) regions show definitive peaks. Both sets of peaks show a proportional rise in the ^{238}U isotope relative to that of ^{235}U. The dose of argon and methane ions also provided a surface that did not produce uranium oxide (251 and 254 AMU) peaks and uranium dioxide (267 and 270 AMU). The absence of uranium oxide and uranium dioxide peaks is consistent with the initial measurements by the Nd:YAG ablation laser through the carbon coating. The lack of oxide molecule formation may be a characteristic of the Nd:YAG ablation laser.

5. Conclusion

Experiments using carbon coating to increase laser ablation efficiency and reduce the surface oxidation of silicate fallout showed successful results. Two historic fallout samples were tested but showed different mass spectra results. The difference in result is most likely accounted for by differences in chemical composition and uranium concentration in the two samples.

Measurements during carbon implantation showed a significant decrease in the uranium oxide and uranium dioxide levels. After initial carbon coating measurements, the cleaning of the carbon coating by argon sputtering may have driven carbon atoms into the surface through inelastic collisions. This unmeasured dose of carbon may have caused the surface reduction. This is also consistent with the fact that Sample 1 produced a strong ion signal in the absence of a carbon coating after Ar^+ cleaning.

V. CONCLUSION

A. CONTRIBUTIONS OF THIS WORK

This thesis presented three separate experimental investigations. First, a COTS CW laser did not pass a feasibility test as a viable replacement for a Ti:Saph pulsed laser in the LION instrument. This null result is directly related to the pulsed nature of the overall LION instrument. While the CW laser provides well over 1 Watt as measured on an average-power meter, LION operates for 1000 measurements for 20 ns each. This means that the power delivered to the LION target chamber is only utilized for 20 micro-seconds. That is why the power as measured by an average-power meter was not an adequate measure of the laser power delivered to the sample being tested. This experiment led to an in-depth understanding of the parameters required in future laser systems.

Next, a new one- and two-color uranium resonance ionization scheme was tested. The scheme was successfully driven to near saturation by the current Ti:Saph lasers. The two-color system also showed the ability to access a low-lying populated state of uranium. Accessing this low-lying population increased the precision of future uranium measurements by accessing an addition 37% of the atomized uranium. Previously, the uranium occupying the low-lying energy states was not resonantly ionized or counted in measurements.

Finally, carbon coating and carbon implantation was used to measure the increased efficiency of laser ablation and surface oxidation reduction due to carbon treatments of the surface of nuclear fallout debris. Carbon coating did increase the laser's ability to transfer heat to the samples and increased the laser ablation efficiency. After transitioning to carbon implantation using methane ions, an increase in the signal-to-noise ratio was achieved. This thesis showed a factor of two increase in the signal-to-noise ratio.

These experiments show continued progress toward optimization methods on the LION RIMS instrument. RIMS is a method for surface measurements that has progressed

with the development of new and better technology over the last forty years. It is currently in a proof-of-concept phase for development as a method for characterizing actinide and other isotope ratios in nuclear materials for safeguards, non-proliferation, and nuclear forensic applications. It shows outstanding potential to develop measurement techniques not achievable by other techniques. It holds the promise of providing early timeline answers at an ever-greater degree of certainty.

This thesis research showed the trial and error of optimization of a laboratory instrument. In my short time working with the LION team at LLNL, development has progressed toward unique resonance ionization schemes, such as those discussed in this thesis, and quantified the high useful yield capable using LION [20]. Given time and further investment, the LION team will provide an instrument capable of contributing at the strategic levels problem sets involving nuclear materials.

B. FUTURE RESEARCH OPPORTUNITIES

1. Continuous Wave Laser Research

Additional research into the use of CW lasers in RIMS should focus on trace element identification. Current COTS CW laser technology is capable of resonance ionization, but does not pair well with a TOF-MS configuration. Research into a one-color two-photon CW uranium instrument for trace detection could offer a potential pathway to a portable and highly automated detection system.

2. Two-Color Uranium Resonance Ionization

An experiment to quantify the relative ionization potentials of the ionization states in the two-color uranium ionization scheme is possible. The ionization states and their associated ionization potential can be measured in the same fashion as in Figure 5 [11]. Using two Ti:Saph lasers initially set to 396 nm with half of the power required for saturation and then scanning one of the lasers would provide a relative ionization potential. A narrow ionization peak would be evidence of an AI state. If the ionization potential does not change significantly with the change in wavelength, it would be evidence of ionization into the continuum. This experiment can provide insight into the coupling between the first

excited state and the ionization state during optical excitation. Quantifying this coupling in both ^{235}U and ^{238}U is essential to quantifying isotopic ratios and any possible laser bias. This experiment is also possible for the 406 nm scheme to confirm or deny a possible Rydberg state below the IP. Modifying the timing of the resonance ion extraction electric field to pulse concurrently with the irradiance of the resonance ionization lasers could increase the ion signal from this possible Rydberg state [8].

3. Carbon Surface Reduction

Future research for carbon implantation should concentrate on silicate samples free of carbon coating treatments. Starting with a sample that has not been treated with any carbon offers a better baseline measurement to compare the effects of carbon implantation. After a baseline measurement, a repeat of this experiment would clarify what caused the reduction of uranium oxide and uranium dioxide in the surface present in previous testing.

THIS PAGE INTENTIONALLY LEFT BLANK

LIST OF REFERENCES

[1] K. Moody, I. Hutcheon, and P. Grant, *Nuclear Forensic Analysis*, Boca Raton, FL: CRC Press, 2005.

[2] J.C. Miller, *Laser Ablation*, Berlin: Springer-Verlag, 1994.

[3] F. Brech and L. Cross, "Optical micromission stimulated by a ruby maser," *Applied Spectroscopy*, vol. 16, no. 2, pp. 59, 1962.

[4] J.P. Young, R.W. Shaw, and D.H. Smith, "Resonance Ionization Mass Spectrometry," A*nalytical Chemistry*, vol. 61, no. 22, pp. 1271A-1279A, Nov. 1989.

[5] C.M. Miller and N.S. Nogar, "Continuous wave Lasers for resonance ionization mass spectrometry," *Analytical Chemistry*, vol. 55, no. 9, pp. 1608–1610, Aug. 1983.

[6] D.L. Donohue, D.H. Smith, J.P. Young, H.S. McKown, and C.A. Pritchard, "Isotopic analysis of uranium and plutonium mixtures by resonance ionization mass spectrometry," *Analytical Chemistry*, vol. 56, no. 3, pp. 379–381, Mar. 1984.

[7] K. Wendt and N. Trautmann, "Recent developments in isotope ratio measurements by resonance ionization mass spectrometry," *International Journal of Mass Spectrometry*, vol. 242, pp. 161–168, 2005.

[8] B.H. Isselhardt, Personal Communications, Sep. 2017.

[9] A. Einstein, "On the quantum theory of radiation," *Phys. Zs.* vol. 18, no. 121. pp. 63–77, Mar. 1917.

[10] V.S. Letokhov, *Laser Photoionization Spectroscopy*, London: Academic Press, 1987.

[11] P.G. Schumann, K.D.A. Wendt, and B.A. Bushaw, "High-resolution triple-resonance autoionization of uranium isotopes," *Spectrochimica Acta Part B*, vol. 60, pp. 1402–1411, 2005.

[12] L.A. Lewis, K.B. Knight, J.E. Matzel, S.G. Prussin, M.M. Zimmer, W.S. Kinman, F.J. Ryerson, and I.D. Hutcheon, "Spatially-resolved analyses of aerodynamic fallout from a uranium fueled nuclear test," *Journal of Environmental Radioactivity*, vol. 148, pp. 183–195, 2015.

[13] D.G. Weisz, "Deposition of vaporized species onto glassy fallout from a near-surface nuclear test," *Geochimica et cosmochimica acta*, vol. 201, pp. 410–426, 2017.

[14] L. Egeberg, "Fallout studies and assessment of radiological phenomena," Civil Effects Test Group, U.S. Naval Radiological Defense Laboratory, San Francisco, CA, Preliminary Report. ITR-1465, Feb. 28, 1958.

[15] M.A. Fitzgerald, K.B. Knight, J.E. Matzel, and K.R. Czerwinski, "Multivariate strategies to modeling source compositions in heterogeneous melt glasses," unpublished.

[16] Z.A. Weinberg, G.W. Rubloff, and E. Bassous, "Transmission, photoconductivity, and the experimental band gap of thermally grown SiO_2 films," *Physics Review B*. vol. 19, no. 6. pp. 3107–3117, Mar. 1979.

[17] W.K. Chu, "Energy loss of charged particles," *in Material Characterization Using Ion* Beams, J.P. Thomas and A. Cachard, Ed. New York: Plenum Press, 1978, pp. 3–34.

[18] G. Blaise, "Fundamental aspects of microanalysis," *in Material Characterization Using Ion* Beams, J.P. Thomas and A. Cachard, Ed. New York: Plenum Press, 1978, pp. 143–238.

[19] P. Sigmund, "Theory of sputtering. I. Sputtering yield of amorphous and polycrystalline targets," *Physical Review*. vol. 184, no. 2. pp. 383–416, Aug. 1969.

[20] M.R. Savina, B.H. Isselhardt, A. Kucher, R. Trappitsch, B.V. King, D. Ruddle, R. Gopal, and I. Hutcheon, "High useful yield and isotopic analysis of uranium by resonance ionization mass spectrometry," *Journal of Analytical Chemistry*, vol. 89, pp. 6224–6231, 2017.

[21] B.H. Isselhardt, "Quantify uranium isotope ratios using resonance ionization Mass spectrometry: the influence of laser parameters on relative ionization Probability," Ph.D. dissertation, Dept. Nuclear Eng., Univ. Cali. Berkeley, Berkeley, CA, 2011.

[22] B.H. Isselhardt, S.G. Prussin, M.R. Savina, D.G. Willingham, K.B. Knight, and I.D. Hutcheon, "Rate equation model of laser induced bias in uranium isotope ratios measured by resonance ionization mass spectrometry." *Journal of Analytical Atomic Spectrometry*, vol. 31, pp. 666–678, 2016.

[23] S.F. Hutchinson, "Modeling of plutonium ionization probabilities for use in nuclear forensic analysis by resonance ionization mass spectrometry," M.S. thesis, Dept. Physics, Naval Postgraduate School, Monterey, CA, 2016.

[24] S.L. Ziegler and B.A. Bushaw, “Ultratrace uranium fingerprinting with isotope selective laser ionization spectrometry,” *Analytical Chemistry*, vol. 80, pp. 6029–6033, 2008.

[25] B.H. Isselhardt, M.R. Savina, A. Kucher, S.D. Gates, K.B. Knight, I.D. Hutcheon, “Improved precision and accuracy in quantifying plutonium isotope ratios by RIMS,” *Journal of Radioanalytical Nuclear Chemistry*, vol. 307, no. 3, pp. 2487–2494, 2016.

[26] R.B. Wright, M.J. Pellin, D.M. Gruen, C.E. Young, “Laser fluorescence spectroscopy of sputtered uranium atoms,” *Nuclear Instruments and Methods*, vol. 170, pp. 295–302, 1980.

[27] W.A. Chupka, “Factors affecting lifetimes and resolution of Ryberg states observed in zero-kinetic-energy spectroscopy,” *Journal of Chemical Physics*, vol. 98, pp. 4520–4530, Mar. 1993.

THIS PAGE INTENTIONALLY LEFT BLANK

INITIAL DISTRIBUTION LIST

1. Defense Technical Information Center
   Ft. Belvoir, Virginia

2. Dudley Knox Library
   Naval Postgraduate School
   Monterey, California